

# Online Research @ Cardiff

This is an Open Access document downloaded from ORCA, Cardiff University's institutional repository: <https://orca.cardiff.ac.uk/id/eprint/113031/>

This is the author's version of a work that was submitted to / accepted for publication.

Citation for final published version:

Khaki, M., Ait-El-Fquih, B., Hoteit, I., Forootan, E. ORCID:  
<https://orcid.org/0000-0003-3055-041X>, Awange, J. and Kuhn, M. 2018.  
Unsupervised ensemble Kalman filtering with an uncertain constraint for land  
hydrological data assimilation. Journal of Hydrology 564 , pp. 175-190.  
10.1016/j.jhydrol.2018.06.080 file

Publishers page: <http://dx.doi.org/10.1016/j.jhydrol.2018.06.080>  
<<http://dx.doi.org/10.1016/j.jhydrol.2018.06.080>>

Please note:

Changes made as a result of publishing processes such as copy-editing, formatting and page numbers may not be reflected in this version. For the definitive version of this publication, please refer to the published source. You are advised to consult the publisher's version if you wish to cite this paper.

This version is being made available in accordance with publisher policies.

See

<http://orca.cf.ac.uk/policies.html> for usage policies. Copyright and moral rights for publications made available in ORCA are retained by the copyright holders.



# Unsupervised Ensemble Kalman Filtering with an Uncertain Constraint for Land Hydrological Data Assimilation

M. Khaki<sup>a,1</sup>, B. Ait-El-Fquih<sup>b</sup>, I. Hoteit<sup>b</sup>, E. Forootan<sup>c</sup>, J. Awange<sup>a</sup>, M. Kuhn<sup>a</sup>

<sup>a</sup>*School of Earth and Planetary Sciences, Discipline of Spatial Sciences, Curtin University, Perth, Australia.*

<sup>b</sup>*King Abdullah University of Science and Technology (KAUST), Thuwal, Saudi Arabia.*

<sup>c</sup>*School of Earth and Ocean Sciences, Cardiff University, Cardiff, UK.*

---

## Abstract

1 The standard ensemble data assimilation schemes often violate the dynamical balances of hydro-  
2 logical models, in particular, the fundamental water balance equation, which relates water storage  
3 and water flux changes. The present study aims at extending the recently introduced Weak Con-  
4 strained Ensemble Kalman Filter (WCEnKF) to a more general framework, namely unsupervised  
5 WCEnKF (UWCEnKF), in which the covariance of the water balance model is no longer known,  
6 thus requiring its estimation along with the model state variables. This extension is introduced  
7 because WCEnKF was found to be strongly sensitive to the (manual) choice of this covariance. The  
8 proposed UWCEnKF, on the other hand, provides a more general unsupervised framework that  
9 does not impose any (manual, thus heuristic) value of this covariance, but suggests an estimation  
10 of it, from the observations, along with the state. The new approach is tested based on numerical  
11 experiments of assimilating Terrestrial Water Storage (TWS) from Gravity Recovery and Climate  
12 Experiment (GRACE) and remotely sensed soil moisture data into a hydrological model. The  
13 experiments are conducted over different river basins, comparing WCEnKF, UWCEnKF, and the  
14 standard EnKF. In this setup, the UWCEnKF constrains the system state variables with TWS  
15 changes, precipitation, evaporation, and discharge data to balance the summation of water storage  
16 simulations. In-situ groundwater and soil moisture measurements are used to validate the results of  
17 the UWCEnKF and to evaluate its performances against the EnKF. Our numerical results clearly  
18 suggest that the proposed framework provides more accurate estimates of groundwater storage  
19 changes and soil moisture than WCEnKF and EnKF over the different studied basins.

**Keywords:** Constrained data assimilation, Ensemble Kalman Filter (EnKF), Unsupervised Weak  
Constrained Ensemble Kalman Filter (UWCEnKF), Water budget closure, Hydrological modeling.

---

*Email address:* Mehdi.Khaki@postgrad.curtin.edu.au (M. Khaki)

<sup>1</sup>Contact details: Department of Spatial Sciences, Curtin University, Perth, Australia, Email: Mehdi.Khaki@postgrad.curtin.edu.au, Tel: 0061410620379

## 20 1. Introduction

21 Hydrological models play important roles in environmental studies and are crucial for hy-  
22 drological applications. Due to a variety of factors, such as model structural errors, data deficiency,  
23 and uncertainty in inputs and parameters, the outputs of these models can be far from perfect.  
24 Data assimilation techniques offer a framework to improve the models simulations by constraining  
25 their outputs to the observations. However, the application of assimilation schemes could intro-  
26 duce an imbalance between water fluxes, namely precipitation  $\mathbf{p}$ , evaporation  $\mathbf{e}$ , discharge  $\mathbf{q}$ , and  
27 changes in water storage,  $\Delta\mathbf{s}$ , through the water balance equation  $\Delta\mathbf{s} = \mathbf{p} - \mathbf{e} - \mathbf{q}$ . The water  
28 balance equation is applied in land hydrological models to describe the relationships between these  
29 fluxes (Sokolov and Chapman, 1974). The model structure governs variations in the water state  
30 changes due to the incoming and outgoing hydrological water fluxes. Data assimilation of any wa-  
31 ter storages, e.g., soil moisture and/or terrestrial water storage (TWS), breaks the existing balance  
32 because the assimilated state does not satisfy the water balance property (Khaki et al., 2017a).

33 Existing data assimilation methodologies under water budget enforcement rely on a “perfect  
34 observations” assumption in the closure constraint (e.g., Pan and Wood, 2006; Sahoo et al., 2011;  
35 Pan et al., 2012). For example, Pan and Wood (2006) proposed a constrained ensemble Kalman  
36 filter (CEnKF) that imposes regional water balance constraint to improve the filtering results.  
37 The CEnKF involves two successive EnKF-like updates. The first update uses the observations  
38 to update the state forecast, following an EnKF-like step, while the second update imposes the  
39 balance constraint via another EnKF-like correction, yet with a different form. Other studies have  
40 applied data merging algorithms along with the CEnKF (see, e.g., Sahoo et al., 2011; Pan et al.,  
41 2012; Zhang et al., 2016) to provide the flux datasets from various resources for water balance  
42 control. Although these improved datasets have resulted in better state estimates over different  
43 river basins by incorporating more accurate information about the constraints, the assumption  
44 of perfect observations is still problematic. This assumption leads to a strong constraint, which  
45 is unrealistic and may cause various issues. Simon and Chia (2002) suggested that even though  
46 it does not present any theoretical problems, the assumption can result in a singular covariance  
47 matrix, which in practice increases the possibility of numerical issues. Furthermore, by neglecting  
48 errors associated with flux observations, one can expect more estimation errors because of the  
49 strong water budget enforcement, which could also lead to over-fitting issues (Tangdamrongsub et  
50 al., 2017).

51 In a recent study, [Khaki et al. \(2017a\)](#) proposed a new two-update ensemble Kalman-based  
52 scheme, a weak constrained ensemble Kalman filter (WCEnKF), that involves uncertainties in the  
53 water budget balance enforcement equation. Unlike previous studies (e.g., [Pan and Wood, 2006](#);  
54 [Sahoo et al., 2011](#); [Pan et al., 2012](#); [Khaki et al., 2017a](#)), water balance uncertainty is added to  
55 the equality constraint formulation, which allows for a more realistic water balance control during  
56 filtering. This has been framed in a supervised framework, i.e., by assigning approximate error  
57 covariance to the water balance observations before filtering, which may not allow for an optimal  
58 estimation of corrections (in the second step of the filter) to be applied to results from the first step  
59 of the filter. The present study aims to extend the work of [Khaki et al. \(2017a\)](#) to the case where  
60 the covariance associated with flux observations is unknown, proposing an unsupervised framework  
61 to estimate it along with the hydrology state variable. The proposed Unsupervised WCEnKF  
62 (UWCEnKF) introduces an iterative scheme in the second update step of the WCEnKF.

63 In order to assess the performance of the UWCEnKF, numerical experiments are carried out  
64 to assimilate the Gravity Recovery And Climate Experiment (GRACE) derived terrestrial wa-  
65 ter storage (TWS), as well as soil moisture products from the Advanced Microwave Scanning  
66 Radiometer-Earth Observing System (AMSR-E) and Soil Moisture and Ocean Salinity (SMOS)  
67 into a hydrological model. Assimilating GRACE TWS data has been performed in a number of  
68 previous studies to constrain the mass balance of hydrological models over different river basins  
69 (e.g., [Zaitchik et al., 2008](#); [van Dijk et al., 2014](#); [Eicker et al., 2014](#); [Reager et al., 2015](#); [Schu-  
70 macher et al., 2016](#); [Khaki et al., 2018a,b](#)). Several studies already demonstrated a great capability  
71 of AMSR-E and SMOS datasets to constrain model estimates through data assimilation (e.g., [De  
72 Jeu et al., 2008](#); [Renzullo et al., 2014](#); [Leroux et al., 2016](#); [Tian et al., 2017](#)). It has also been shown  
73 that simultaneous assimilation of the different datasets generally leads to better results in terms of  
74 state estimates (e.g., [Zhang et al., 2014](#); [Renzullo et al., 2014](#); [Han et al., 2016](#); [Tian et al., 2017](#);  
75 [Lievens et al., 2017](#)) as compared to individual assimilation of the different datasets. This motivates  
76 the current study to simultaneously assimilate GRACE TWS and soil moisture observations from  
77 AMSR-E and SMOS. We also apply the standard EnKF to compare its results with the proposed  
78 UWCEnKF filter. This enables to evaluate the relevance of the proposed approach for enforcing  
79 the water budget closure.

80 We further consider multiple observations of the water components in the water budget equation.  
81 This is done to achieve the best estimates of  $\mathbf{p}$  and  $\mathbf{e}$  over different basins (see Figure 1). Multi-

mission products for precipitation and evaporation are used in the data merging approach of [Sahoo et al. \(2011\)](#) to derive a single data set for each observation type (i.e.,  $\mathbf{p}$  and  $\mathbf{e}$ ). The approach estimates uniform datasets independently for each basin. The merged data, as well as the water discharge measurements from various ground stations, are then applied to constrain the water balance equation in the UWCEnKF’s second update. This experiment is undertaken over eight globally distributed basins; Amazon, Indus, Mississippi, Orange, Danube, St. Lawrence, Murray-Darling, and the Yangtze, to better explore the capability of the proposed filter.

The remainder of the paper is organized as follows. We first describe the data and model in Section 2. The UWCEnKF algorithm and experiments set up are described in Sections 3 and 4, respectively. We illustrate and discuss the experiments results in Section 5 and conclude the study in Section 6.

## 2. Model and data

### 2.1. Hydrological model

Vertical water compartments of the globally distributed World-Wide Water Resources Assessment system (W3RA) model, developed in 2008 by the Commonwealth Scientific and Industrial Research Organisation (CSIRO; Australia), are used to simulate water storages. W3RA is a one-dimensional system that simulates landscape water stored in the vegetation and soil systems ([van Dijk, 2010](#)). Here, we use the  $1^\circ \times 1^\circ$  version of the model to represent the water balance of the soil, groundwater and surface water storage, in which each cell is modeled independently from its neighbors ([van Dijk, 2010](#)). Groundwater dynamics in the model includes recharge from deep drainage, capillary rise (estimated with a linear diffusion equation), evaporation from groundwater saturated areas, and discharge. The model assumes that redistribution between grid cells can be ignored. Groundwater and river water dynamics are simulated at grid cell level and hence parameters are equal across the grid cell. Meteorological data sets of minimum and maximum temperature, downwelling short-wave radiation, and precipitation products provided by Princeton University (<http://hydrology.princeton.edu>) are used to force the W3RA model between 2003 and 2013. The model state is composed of the top, shallow and deep root soil water, snow, vegetation, groundwater, and surface water storage.

## 2.2. Assimilated observations

Observations are assimilated in two steps. The first step assimilates GRACE TWS and satellite soil moisture observations, which are used to update the forecast state, while the second step enforces the water balance constraints, based on water flux observations.

### 2.2.1. Data used in the first update

GRACE level 2 (L2) gravity field data provided by the ITSG-Grace2016 (Mayer-Gürr et al., 2014) is used to compute monthly TWS after applying a few standard corrections. These include replacing degree 1 (C10, C11, S11) and degree 2 (C20) coefficients by more accurate coefficients from Swenson et al. (2008) and the Satellite Laser Ranging solutions (Cheng and Tapley, 2004), respectively. The gravity fields are then converted to  $3^\circ \times 3^\circ$  TWS fields (Wahr et al., 1998). Khaki et al. (2017b) showed that implementing GRACE TWS with this spatial resolution exploits better impacts of GRACE TWS mainly because of larger correlation errors in the higher spatial resolution fields, which can be problematic during assimilation (see also Eicker et al., 2014; Schumacher et al., 2016). Colored/correlated noise and leakage errors are reduced using the Kernel Fourier Integration (KeFIn) filter, as proposed by Khaki et al. (2018c). The KeFIn filter works through a two-step post-processing algorithm: in the first step it mitigates the measurement noise and the aliasing of unmodelled high-frequency mass variations, and in the second step it decreases the leakage errors. Note that, here, rather using model outputs, fixed signal to noise ratio is applied during the KeFIn filtering (see Khaki et al., 2018c, for details). The application of the KeFIn filter was shown in Khaki et al. (2018c) to outperform a number of existing GRACE filtering techniques, e.g., land-grid-scaling method applied in Mass Concentration blocks (Mascons) products justifying its use in the current study.

Furthermore, soil moisture products from the Advanced Microwave Scanning Radiometer for EOS (AMSR-E) and ESA’s Soil Moisture Ocean Salinity (SMOS) Earth Explorer mission are used to update soil storage variations. AMSR-E measures surface brightness temperature that corresponds to surface soil moisture content of 2 cm depth (Njoku et al., 2003). SMOS, on the other hand, measures microwave emissions from Earth’s surface at about 5 cm depth. Here we use descending passes (see, e.g., De Jeu and Owe, 2003) of gridded Level-3 land surface product AMSR-E (Njoku, 2004) between 2003 and 2011, and Level 3 CATDS (Centre Aval de Traitement des Donnees SMOS) on ascending passes (see, e.g., Draper et al., 2009) for the period of 2011



to 2013. These passes are selected due to their higher agreement with in-situ measurements (see also [Jackson and Bindlish, 2012](#); [Su et al., 2013](#)). Both data products are rescaled to a monthly  $1^\circ \times 1^\circ$  scale for the present study. Cumulative distribution function (CDF) matching ([Reichle and Koster, 2004](#); [Drusch et al., 2005](#)) is applied to rescale the observations and remove the bias between the model simulations and observations. These measurements are mainly used to constrain the model variability, and not its absolute values. CDF matching relies on the assumption that the difference between observed soil moisture and that of the model is stationary and guarantees that the statistical distribution of both time series is the same ([Draper et al., 2009](#); [Renzullo et al., 2014](#)).

### 2.2.2. Data used in the second update

Multiple data sets are used for flux net observations. Details of these products are outlined in Table 1. For precipitation, we use the Tropical Rainfall Measuring Mission (TRMM-3B43; [Huffman et al., 2007](#)), NOAA CPC Morphing Technique (CMORPH; [Joyce et al., 2004](#)), the Global Precipitation Climatology Project (GPCP) Version 2.3 ([Adler et al., 2003](#)), Global Precipitation Climatology Centre (GPCC; [Schneider et al., 2008](#)), and CPC unified gauge dataset ([Chen et al., 2002](#)). TRMM-3B43, CMORPH, and GPCP are used to generate the merged precipitation for data assimilation, while GPCC and CPC are applied for uncertainty analysis (cf. Section 4.1). Evaporation data are collected from MODIS Global Evapotranspiration Project (MOD16; [Mu et al., 2007](#)), Global Land Evaporation Amsterdam Model (GLEAM; [Miralles et al., 2011](#)), ERA-interim ([Simmons et al., 2007](#)), and Variable Infiltration Capacity (VIC) land surface model ([Liang et al., 1994](#)). Similar to precipitation, an uncertainty analysis is undertaken for evaporation with respect to ERA-interim and VIC products. All of these products are rescaled into a monthly  $1^\circ \times 1^\circ$  spatial resolution. Various data sources are considered for discharge (see Table 1) to achieve the maximum amount of coverage within the basins of Amazon, Indus, Mississippi, Orange, Danube, St. Lawrence, Murray-Darling, and Yangtze (Figure 1).

FIGURE 1

### 2.3. In-situ measurements

Monthly in-situ groundwater and soil moisture measurements are used to validate the results. The groundwater stations are located in the Mississippi, St. Lawrence, and Murray-Darling basins. Specific yield values provided by the literature (e.g., [Gutentag et al., 1984](#); [Strassberg et al., 2007](#); [Seoane et al., 2013](#); [Khaki et al., 2017a](#)) are used to convert well measurements into groundwater storage anomalies. We further use in-situ soil moisture measurements over the Mississippi, St. Lawrence, Danube, Yangtze, and Murray-Darling basins to assess the estimated soil moisture. These data are collected from the International Soil Moisture Network (ISMN) and the moisture-monitoring network. It is worth mentioning that the temporal averages from the in-situ time series are removed before using them to validate the assimilation results. The distribution of both groundwater and soil moisture in-situ products are displayed in Figure 1. Details of the datasets are outlined in Table 1.

TABLE 1

## 3. Methodology

### 3.1. Problem formulation

Our discrete-time state-space system is represented as,

$$\begin{cases} \mathbf{x}_t &= \mathcal{M}_{t-1}(\mathbf{x}_{t-1}) + \nu_t, \\ \mathbf{y}_t &= \mathbf{H}_t \mathbf{x}_t + \mathbf{w}_t, \end{cases} \quad (1)$$

where  $\mathbf{x}_t \in \mathbb{R}^{n_x}$  and  $\mathbf{y}_t \in \mathbb{R}^{n_y}$  stand for the system state and the observation at time  $t$  and of sizes  $n_x$  and  $n_y$ , respectively. In system (1),  $\mathcal{M}_{t-1}(\cdot)$  is a nonlinear operator integrating the system state from time  $t-1$  to  $t$ , and  $\mathbf{H}_t$  is the observational (design) operator at time  $t$ , which is linear in our application. Note, however, that the proposed scheme can be easily extended to the nonlinear case ([Liu and Xue, 2002](#)). The model process noise,  $\nu = \{\nu_t\}_{t=0}^T$ , and the observation process noise,  $\mathbf{w} = \{\mathbf{w}_t\}_{t=0}^T$ , are assumed to be independent in time, jointly independent, and independent of the initial state, shown by  $\mathbf{x}_0$ . Furthermore,  $\nu_t$  and  $\mathbf{w}_t$  are assumed to be Gaussian with zero means and covariances  $\mathbf{Q}_t$  and  $\mathbf{R}_t$ , respectively. The model time step,  $t$ , is considered to be equal to the



assimilation time step. More details about the state-space formulation (i.e., about the structures of  $\mathbf{x}_t$ ,  $\mathbf{y}_t$ ,  $\mathcal{M}_t$  and  $\mathbf{H}_t$ ) of our application can be found in [Khaki et al. \(2017a\)](#).

The ensemble Kalman filter update step does not constrain the water fluxes and this likely distorts their balance ( $\Delta \mathbf{s} = \mathbf{p} - \mathbf{e} - \mathbf{q}$ ). This was enforced by [Khaki et al. \(2017a\)](#), up to a weak constraint:

$$\mathbf{d}_t = -\mathbf{x}_t + \mathbf{x}_{t-1} + \mathbf{p}_t - \mathbf{e}_t - \mathbf{q}_t + \boldsymbol{\xi}_t, \quad (2)$$

accounting for the uncertainty in the different water fluxes data through a noise term  $\boldsymbol{\xi}_t$ , which we assume here to be Gaussian with zero mean and covariance,  $\boldsymbol{\Sigma}$ , and independent of  $\boldsymbol{\xi}_{t' \neq t}$ ,  $\{\nu_t\}_{t=0}^T$ ,  $\{\mathbf{w}_t\}_{t=0}^T$  and  $\mathbf{x}_0$ . Considering Eq. (2), one can see that changes in the water storage at two successive time steps is equal to the difference between precipitation and summation of evaporation and discharge up to uncertainties in the involved data. The constraint in Eq. (2) can be rewritten as another observation equation in the state-space formulation, Eq. (3), which also involves the state at the previous time,

$$\mathbf{z}_t = \mathbf{G}\mathbf{x}_t + \mathbf{L}\mathbf{x}_{t-1} + \boldsymbol{\xi}_t, \quad (3)$$

where  $\mathbf{z}_t \stackrel{\text{def}}{=} \mathbf{d}_t - \mathbf{p}_t + \mathbf{e}_t + \mathbf{q}_t$  plays the role of a “pseudo-observation”,  $\mathbf{L}$  is an  $n_z \times n_x$  identity matrix, and  $\mathbf{G} = -\mathbf{L}$  (here,  $n_z = n_x$ ). Define  $\mathbf{r}_t = [\mathbf{y}_t^T, \mathbf{z}_t^T]^T$  and  $\mathbf{r}_{0:t} = \{\mathbf{r}_0, \mathbf{r}_1, \dots, \mathbf{r}_t\}$ . In the state-space system (1)-(3), a generic filtering algorithm has been recently introduced by [Khaki et al. \(2017a\)](#), recursively computing the analysis pdf of the state  $\mathbf{x}_t$  from the history of the augmented observations,  $\mathbf{r}_{0:t}$ ,  $p(\mathbf{x}_t | \mathbf{r}_{0:t})$ . The computation of  $p(\mathbf{x}_t | \mathbf{r}_{0:t})$  from  $p(\mathbf{x}_{t-1} | \mathbf{r}_{0:t-1})$  proceeds in a succession of a forecast step and two Bayesian update steps. The forecast step consists of moving from  $p(\mathbf{x}_{t-1} | \mathbf{r}_{0:t-1})$  to the forecast pdf,  $p(\mathbf{x}_t | \mathbf{r}_{0:t-1})$ , based on the state transition pdf  $p(\mathbf{x}_t | \mathbf{x}_{t-1})$  (which is described by the state model). The resulting forecast pdf is then updated, based on the likelihood of the observations,  $p(\mathbf{y}_t | \mathbf{x}_t)$  (which is represented by the observation model), resulting in an unconstrained analysis pdf<sup>2</sup>,  $p(\mathbf{x}_t | \mathbf{r}_{0:t-1}, \mathbf{y}_t)$ . The latter is, in turn, updated in the second Bayesian step, based on the likelihood of the pseudo-observation,  $p(\mathbf{z}_t | \mathbf{x}_{t-1}, t)$  (which is represented by the constraint Eq. (3)), leading to the desirable analysis pdf at the current time  $t$ ,  $p(\mathbf{x}_t | \mathbf{r}_{0:t})$ . Details about these steps can be found in ([Khaki et al., 2017a](#)).

In a supervised framework, where the parameters of the constrained state-space system (includ-

---

<sup>2</sup>The term *unconstrained* comes from the fact that these pdfs are not based on the pseudo-observation,  $\mathbf{z}_t$ , that “represents” the equality constraint.

ing  $\Sigma$ ) are known, the above generic algorithm was implemented by [Khaki et al. \(2017a\)](#) through Monte Carlo approximation of the posterior mean (PM) estimate of the state and its covariance, which led to the ensemble Kalman-type WCEnKF. [Khaki et al. \(2017a\)](#) noticed that the WCEnKF is sensitive to the choice of  $\Sigma$ , which can strongly affect the filter behaviors. Here, we design a more general unsupervised framework in which  $\Sigma$  is an unknown diagonal covariance matrix, which thereby needs to be estimated concurrently with the state.

### 3.2. The Unsupervised Weak Constrained Ensemble Kalman Filter (UWCEnKF)

#### 3.2.1. The generic algorithm

The UWCEnKF shares the same forecast and first update steps as the WCEnKF, but computes the posterior distribution of both state and pseudo-observation noise covariance in the second update step, instead of only that of the state. In a Bayesian framework, this consists in viewing the covariance,  $\Sigma$ , as another random variable with a given prior pdf; the goal is then to compute its posterior pdf jointly with the state<sup>3</sup>,  $p(\mathbf{x}_{t-1}, \mathbf{x}_t, \Sigma | \mathbf{r}_{0:t})$ . However, the statistical dependencies between the states,  $\mathbf{x}_{t-1:t}$ , and the covariance,  $\Sigma$ , makes its computation quite tricky. One way to overcome this difficulty is to resort to the variational Bayesian (VB) approach and approximate  $p(\mathbf{x}_{t-1}, \mathbf{x}_t, \Sigma | \mathbf{r}_{0:t})$  with a separable pdf  $q(\mathbf{x}_{t-1}, \mathbf{x}_t, \Sigma | \mathbf{r}_{0:t}) = q(\mathbf{x}_{t-1}, \mathbf{x}_t | \mathbf{r}_{0:t})q(\Sigma | \mathbf{r}_{0:t})$ , under the Kullback-Leibler divergence (KLD) minimization criteria ([Jaakkola and Jordan, 2000](#); [Smidl and Quinn, 2008](#); [Ait-El-Fquih and Hoteit, 2015, 2016](#)). This reads,

$$\begin{aligned} q(\mathbf{x}_{t-1}, \mathbf{x}_t, \Sigma | \mathbf{r}_{0:t}) &= \underset{\phi(\mathbf{x}_{t-1}, \mathbf{x}_t, \Sigma | \mathbf{r}_{0:t})}{\operatorname{argmin}} \operatorname{KLD}(\phi(\mathbf{x}_{t-1}, \mathbf{x}_t, \Sigma | \mathbf{r}_{0:t}) || p(\mathbf{x}_{t-1}, \mathbf{x}_t, \Sigma | \mathbf{r}_{0:t})), \\ &= \underset{\phi(\mathbf{x}_{t-1}, \mathbf{x}_t, \Sigma | \mathbf{r}_{0:t})}{\operatorname{argmin}} \mathbb{E}_{\phi(\mathbf{x}_{t-1}, \mathbf{x}_t, \Sigma | \mathbf{r}_{0:t})} \left[ \ln \left( \frac{\phi(\mathbf{x}_{t-1}, \mathbf{x}_t, \Sigma | \mathbf{r}_{0:t})}{p(\mathbf{x}_{t-1}, \mathbf{x}_t, \Sigma | \mathbf{r}_{0:t})} \right) \right], \end{aligned} \quad (4)$$

where  $\mathbb{E}_{\phi(u)}[f(u)]$  denotes the expected value of  $f(u)$  with respect to (w.r.t.) the pdf  $\phi(u)$ . The solution of Eq. (4) can be obtained from (the proof can be found for instance in [Smidl and Quinn, 2006](#), pages 28-31):

$$q(\mathbf{x}_{t-1}, \mathbf{x}_t | \mathbf{r}_{0:t}) \propto \exp \left( \mathbb{E}_{q(\Sigma | \mathbf{r}_{0:t})} [\ln (p(\mathbf{x}_{t-1}, \mathbf{x}_t, \Sigma, \mathbf{r}_{0:t}))] \right), \quad (5)$$

$$q(\Sigma | \mathbf{r}_{0:t}) \propto \exp \left( \mathbb{E}_{q(\mathbf{x}_{t-1}, \mathbf{x}_t | \mathbf{r}_{0:t})} [\ln (p(\mathbf{x}_{t-1}, \mathbf{x}_t, \Sigma, \mathbf{r}_{0:t}))] \right). \quad (6)$$

---

<sup>3</sup>For the sake of clarity, the inclusion of both  $\mathbf{x}_t$  and  $\mathbf{x}_{t-1}$  in the joint posterior pdf of interest is due to the fact that both these states appear in the pseudo-observation model Eq. (3), which necessitates estimating both of them.

According to Eqs. (5) and (6), the independence that is inserted between the marginal posteriors,  $q(\mathbf{x}_{t-1}, \mathbf{x}_t | \mathbf{r}_{0:t})$  and  $q(\mathbf{\Sigma} | \mathbf{r}_{0:t})$ , is partially compensated by the fact that each of these pdfs remains dependent on the expected value of  $\ln(p(\mathbf{x}_{t-1}, \mathbf{x}_t, \mathbf{\Sigma}, \mathbf{r}_{0:t}))$  w.r.t. the other. However, this property of “cyclic” dependence between  $q(\mathbf{x}_{t-1}, \mathbf{x}_t | \mathbf{r}_{0:t})$  and  $q(\mathbf{\Sigma} | \mathbf{r}_{0:t})$  makes it impossible to exactly evaluate these pdfs, or any of their statistics, such as for instance their means, which are taken as the PM estimates of the states and the covariance,  $\mathbf{\Sigma}$ , respectively. A standard approximation is to proceed with cyclic iterations between (5) and (6), evaluating one pdf after the other, until convergence is reached (Smidl and Quinn, 2008; Sato, 2001; Massoud et al., 2018). Based on the factorization,

$$p(\mathbf{x}_{t-1}, \mathbf{x}_t, \mathbf{\Sigma}, \mathbf{r}_{0:t}) \propto p(\mathbf{z}_t | \mathbf{x}_{t-1}, \mathbf{x}_t, \mathbf{\Sigma}) p(\mathbf{x}_{t-1}, \mathbf{x}_t | \mathbf{r}_{0:t-1}, \mathbf{y}_t) q(\mathbf{\Sigma} | \mathbf{r}_{0:t-1}), \quad (7)$$

which stems from the conditional independence properties of the state-space system (1)-(3), the iterative form of Eqs. (5)-(6) becomes,

$$q^{(\ell)}(\mathbf{x}_{t-1}, \mathbf{x}_t | \mathbf{r}_{0:t}) \propto \exp \left( \mathbb{E}_{q^{(\ell-1)}(\mathbf{\Sigma} | \mathbf{r}_{0:t})} \left[ \ln \left( p^{(\ell-1)}(\mathbf{z}_t | \mathbf{x}_{t-1}, \mathbf{x}_t, \mathbf{\Sigma}) \right) \right] \right) p(\mathbf{x}_{t-1}, \mathbf{x}_t | \mathbf{r}_{0:t-1}, \mathbf{y}_t), \quad (8)$$

$$q^{(\ell)}(\mathbf{\Sigma} | \mathbf{r}_{0:t}) \propto \exp \left( \mathbb{E}_{q^{(\ell)}(\mathbf{x}_{t-1}, \mathbf{x}_t | \mathbf{r}_{0:t})} \left[ \ln \left( p^{(\ell-1)}(\mathbf{z}_t | \mathbf{x}_{t-1}, \mathbf{x}_t, \mathbf{\Sigma}) \right) \right] \right) q(\mathbf{\Sigma} | \mathbf{r}_{0:t-1}), \quad (9)$$

where  $p^{(\ell)}(\cdot)$  and  $q^{(\ell)}(\cdot)$  respectively denote the pdfs  $p(\cdot)$  and  $q(\cdot)$  at iteration  $\ell$ . As can be seen below (cf. Section 3.2.2), iterating over the pdfs Eqs. (8)-(9) amounts in practice to iterate over their (approximate) parameters, thereby leading to an unsupervised ensemble-based filtering scheme, which iterates in its second step over the PM estimates of the states and the pseudo-observation noise covariance.

### 3.2.2. Practical implementation

For the sake of simplicity, we first focus on the case of a homogeneous noise with a covariance matrix,

$$\mathbf{\Sigma} = \lambda \times \mathbb{I}_{n_z}, \quad (10)$$

where  $\lambda$  is the variance value and  $\mathbb{I}_{n_z}$  denotes the  $n_z \times n_z$  identity matrix. The more general inhomogeneous case will be discussed later. The prior probability distribution  $p(\lambda)$  is chosen as an inverse-Gamma distribution (as a natural choice for variances), with shape and scale parameters  $\hat{\alpha}_0$  and  $\hat{\beta}_0$ , respectively (Smidl and Quinn, 2006). In the case of non-informative priors, one could take  $\hat{\alpha}_0 = \hat{\beta}_0$  relatively small. At each iteration  $(\ell - 1) \rightarrow (\ell)$ , inserting in Eqs. (8) and (9) the

258 Gaussian pdf,

$$p^{(\ell-1)}(\mathbf{z}_t | \mathbf{x}_{t-1}, \mathbf{x}_t, \boldsymbol{\Sigma}) = \mathcal{N}_{\mathbf{z}_t}(\mathbf{G}\mathbf{x}_t + \mathbf{L}\mathbf{x}_{t-1}, \boldsymbol{\Sigma}^{(\ell-1)}),$$

259 one obtains a posterior  $q^{(\ell)}(\lambda | \mathbf{r}_{0:t})$  that is also an inverse-Gamma distribution with parameters,  $\hat{\alpha}_t$   
 260 and  $\hat{\beta}_t^{(\ell)}$ , given in Eqs. (17)-(18) below. Likewise,  $q^{(\ell)}(\mathbf{x}_{t-1}, \mathbf{x}_t | \mathbf{r}_{0:t})$  is Gaussian with an ensemble  
 261 representation given in Eqs. (14)-(16).

262 **The UWCEnKF.** Starting at time  $t - 1$  from an analysis ensemble,  $\{\mathbf{x}_{t-1}^{a,(i)}\}_{i=1}^m$ , and shape and  
 263 scale parameters  $(\hat{\alpha}_{t-1}, \hat{\beta}_{t-1})$  of the inverse-Gamma posterior pdf  $p(\lambda | \mathbf{r}_{0:t-1})$ , these at the next  
 264 time  $t$  can be computed following a succession of a forecast and two update steps. The forecast  
 265 step, which computes the forecast ensemble,  $\{\mathbf{x}_t^{f,(i)}\}_{i=1}^m$ , and the first update step (with  $\mathbf{y}_t$ ), which  
 266 computes the unconstrained analysis and smoothing ensembles,  $\{\tilde{\mathbf{x}}_t^{a,(i)}\}_{i=1}^m$  and  $\{\tilde{\mathbf{x}}_{t-1}^{s,(i)}\}_{i=1}^m$ , are  
 267 identical to those in Khaki et al. (2017a), namely,

$$\mathbf{x}_t^{f,(i)} = \mathcal{M}_{t-1}(\mathbf{x}_{t-1}^{a,(i)}) + \nu^{(i)}, \quad (11)$$

$$\tilde{\mathbf{x}}_t^{a,(i)} = \mathbf{x}_t^{f,(i)} + \mathbf{P}_{\mathbf{x}_t^f} \mathbf{H}^T \underbrace{[\mathbf{H} \mathbf{P}_{\mathbf{x}_t^f} \mathbf{H}^T + \mathbf{R}_t]^{-1} [\mathbf{y}_t + \epsilon^{(i)} - \mathbf{H} \mathbf{x}_t^{f,(i)}]}_{\mu_t^{(i)}}, \quad (12)$$

$$\tilde{\mathbf{x}}_{t-1}^{s,(i)} = \mathbf{x}_{t-1}^{a,(i)} + \mathbf{P}_{\mathbf{x}_{t-1}^a, \mathbf{x}_t^f} \mathbf{H}^T \times \mu_t^{(i)}, \quad (13)$$

268 where  $\mathbf{P}_{\mathbf{x}_t^f}$  is the sample forecast error covariance and  $\mathbf{P}_{\mathbf{x}_{t-1}^a, \mathbf{x}_t^f}$  represents the sample cross-covariance  
 269 between the previous analysis and current forecast errors,  $\nu^{(i)} \sim \mathcal{N}(\mathbf{0}, \mathbf{Q}_t)$ , and  $\epsilon^{(i)} \sim \mathcal{N}(\mathbf{0}, \mathbf{R}_t)$ .

270 As for the second update step (with  $\mathbf{z}_t$ ), which applies the adjustment to enforce the water  
 271 budget balance constraint, it involves iterations to compute Eqs. (8)-(9). Let  $\hat{\alpha}_t = \hat{\alpha}_{t-1} + \frac{n_z}{2}$ ,  
 272 the iteration begins with the initialization  $\hat{\lambda}_t^{(0)} = \frac{\hat{\beta}_{t-1}}{\hat{\alpha}_t}$  and correspondingly  $\hat{\boldsymbol{\Sigma}}_t^{(0)} = \hat{\lambda}_t^{(0)} \times \mathbb{I}_{n_z}$ . For  
 273  $\ell = 0 \cdots L$ , the state members are first updated as,

$$\mathbf{z}_t^{f,(i,\ell)} = \mathbf{G} \tilde{\mathbf{x}}_t^{a,(i)} + \mathbf{L} \tilde{\mathbf{x}}_{t-1}^{s,(i)} + \boldsymbol{\xi}_t^{(i,\ell)}; \quad \boldsymbol{\xi}_t^{(i,\ell)} \sim \mathcal{N}(\mathbf{0}, \hat{\boldsymbol{\Sigma}}_t^{(\ell)}), \quad i = 1, \dots, m, \quad (14)$$

$$\mathbf{x}_t^{a,(i,\ell)} = \tilde{\mathbf{x}}_t^{a,(i)} + \mathbf{P}_{\tilde{\mathbf{x}}_t^a, \mathbf{z}_t^{f,\ell}} \underbrace{[\mathbf{M} \mathbf{P}_{\boldsymbol{\eta}_t} \mathbf{M}^T + \hat{\boldsymbol{\Sigma}}_t^{(\ell)}]^{-1} [\mathbf{z}_t - \mathbf{z}_t^{f,(i,\ell)}]}_{\nu_t^{(i,\ell)}}, \quad i = 1, \dots, m, \quad (15)$$

$$\mathbf{x}_{t-1}^{s,(i,\ell)} = \tilde{\mathbf{x}}_{t-1}^{s,(i)} + \mathbf{P}_{\tilde{\mathbf{x}}_{t-1}^s, \mathbf{z}_t^{f,\ell}} \times \nu_t^{(i,\ell)}, \quad i = 1, \dots, m, \quad (16)$$

274 where  $\mathbf{M} \stackrel{\text{def}}{=} [\mathbf{G}, \mathbf{L}]$ ;  $\mathbf{P}_{\tilde{\mathbf{x}}_t^a, \mathbf{z}_t^{f,\ell}}$  and  $\mathbf{P}_{\tilde{\mathbf{x}}_{t-1}^s, \mathbf{z}_t^{f,\ell}}$  are the sample cross-covariances computed using the

ensembles  $\{\tilde{\mathbf{x}}_t^{a,(i)}\}_{i=1}^m$ ,  $\{\tilde{\mathbf{x}}_{t-1}^{s,(i)}\}_{i=1}^m$  and  $\{\tilde{\mathbf{x}}_t^{f,(i,\ell)}\}_{i=1}^m$ ; and  $\mathbf{P}_{\boldsymbol{\eta}_t}$  is the sample covariance of the ensemble  $\{\boldsymbol{\eta}_t^{(i)}\}_{i=1}^m$  with  $\boldsymbol{\eta}_t^{(i)} \stackrel{\text{def}}{=} [(\tilde{\mathbf{x}}_t^{a,(i)})^T, (\tilde{\mathbf{x}}_{t-1}^{s,(i)})^T]^T$ . Based on the resulting ensembles, the observation noise variance is then updated as,

$$\hat{\beta}_t^{(\ell+1)} = \hat{\beta}_{t-1} + \frac{1}{2}[\|\mathbf{z}_t - \mathbf{G}\hat{\mathbf{x}}_t^{a,(\ell)} - \mathbf{L}\hat{\mathbf{x}}_{t-1}^{s,(\ell)}\|^2 + \text{Trace}(\mathbf{M}\mathbf{P}_{\boldsymbol{\gamma}_t^\ell}\mathbf{M}^T)], \quad (17)$$

$$\hat{\lambda}_t^{(\ell+1)} = \hat{\beta}_t^{(\ell+1)} / \hat{\alpha}_t, \quad (18)$$

$$\hat{\Sigma}_t^{(\ell+1)} = \hat{\lambda}_t^{(\ell+1)} \times \mathbb{I}_{n_z}, \quad (19)$$

where  $\hat{\mathbf{x}}_t^{a,(\ell)}$  and  $\hat{\mathbf{x}}_{t-1}^{s,(\ell)}$  are the (empirical) means of the ensembles  $\{\mathbf{x}_t^{a,(i,\ell)}\}_{i=1}^m$  and  $\{\mathbf{x}_{t-1}^{s,(i,\ell)}\}_{i=1}^m$ , respectively; and  $\mathbf{P}_{\boldsymbol{\gamma}_t^\ell}$  is the sample covariance of the ensemble  $\{\boldsymbol{\gamma}_t^{(i,\ell)}\}_{i=1}^m$  with  $\boldsymbol{\gamma}_t^{(i,\ell)} \stackrel{\text{def}}{=} [(\mathbf{x}_t^{a,(i,\ell)})^T, (\mathbf{x}_{t-1}^{s,(i,\ell)})^T]^T$ . The  $\hat{\Sigma}_t^{(L)}$  and  $\{\mathbf{x}_t^{a,(i,L)}\}_{i=1}^m$  are then considered as the analysis covariance and state estimates, respectively, that will be used in the next assimilation cycle. In our numerical experiments, only few iterations (less than 10) were needed to reach convergence based on the variance estimate. Note that instead of pre-setting the number of iterations,  $L$ , one may use an alternative stopping criteria based, for instance, on the relative squared error norm (RSEN) of the estimated state and/or variance(s), or the evidence lower bound (ELB), defined as (Blei et al. , 2017),

$$\mathcal{E}_1 = \mathbb{E}_{q(\boldsymbol{\xi}_t, \boldsymbol{\Sigma} | \mathbf{r}_{0:t})}[\ln(p(\mathbf{v}_t, \boldsymbol{\Sigma}, \mathbf{r}_t | \mathbf{r}_{0:t-1}))] - \mathbb{E}_{q(\boldsymbol{\xi}_t, \boldsymbol{\Sigma} | \mathbf{r}_{0:t})}[\ln(q(\mathbf{v}_t, \boldsymbol{\Sigma} | \mathbf{r}_{0:t}))], \quad (20)$$

with  $\mathbf{v}_t = [\mathbf{x}_t^T, \mathbf{x}_{t-1}^T]^T$ . Note that it is not possible to use the KLD as this requires the knowledge of the target pdf,  $p(\mathbf{v}_t, \boldsymbol{\Sigma} | \mathbf{r}_{0:t})$ , which, indeed, is not known. Furthermore, minimizing the KLD amounts to maximizing the ELB (Blei et al. , 2017). However, a problem occurs in practice with ELB (20) in case of large dimensional systems (i.e., when  $n_x > m$ ). In such a case, the covariance  $\mathbf{P}_{\boldsymbol{\gamma}_t}$ , whose inverse is involved in the expression of the (assumed Gaussian) pdf,  $q(\mathbf{v}_t | \mathbf{r}_{0:t})$ , is a low-rank matrix, and thus not invertible. To overcome this limitation, we propose to remove the variable,  $\mathbf{v}_t$ , from the ELB, by rather using pdfs that are conditional on this variable (i.e., for which  $\mathbf{v}_t$  is a fixed known value). Since the iterations' process occurs in the second update step (i.e., which uses  $\mathbf{z}_t$ ), we assign to  $\mathbf{v}_t$  the mean  $\hat{\boldsymbol{\eta}}_t$  of  $\{\boldsymbol{\eta}_t^{(i)}\}_{i=1}^m$ , which, indeed, is an approximation of  $\mathbb{E}_{q(\boldsymbol{\xi}_t | \mathbf{r}_{0:t-1}, \mathbf{y}_t)}[\mathbf{v}_t]$  (i.e., the unconstrained analysis mean of  $\mathbf{v}_t$ ). The resulting ELB reads,

$$\begin{aligned} \mathcal{E}_2 &= \mathbb{E}_{q(\boldsymbol{\Sigma} | \mathbf{r}_{0:t})}[\ln(p(\boldsymbol{\Sigma}, \mathbf{r}_t | \mathbf{r}_{0:t-1}, \hat{\boldsymbol{\eta}}_t))] - \mathbb{E}_{q(\boldsymbol{\Sigma} | \mathbf{r}_{0:t})}[\ln(q(\boldsymbol{\Sigma} | \mathbf{r}_{0:t}))], \\ &\approx \text{cte} + \mathbb{E}_{q(\boldsymbol{\Sigma} | \mathbf{r}_{0:t})}[\ln(p(\mathbf{z}_t | \boldsymbol{\Sigma}, \hat{\boldsymbol{\eta}}_t))] + \mathbb{E}_{q(\boldsymbol{\Sigma} | \mathbf{r}_{0:t})}[\ln(q(\boldsymbol{\Sigma} | \mathbf{r}_{0:t-1}))] - \mathbb{E}_{q(\boldsymbol{\Sigma} | \mathbf{r}_{0:t})}[\ln(q(\boldsymbol{\Sigma} | \mathbf{r}_{0:t}))], \end{aligned} \quad (21)$$

where the term “cte” encompasses all the terms that do not depend on  $\Sigma$ . This suggests that the convergence of the proposed scheme can be monitored based either on the change in  $\mathcal{E}_2$  only, the change in RSEN of the state only, the change in  $\mathcal{E}_2$  and RSEN of the state, or, as stated above, the change in RSEN of both state and  $\Sigma$ . Finally, based on the Gaussian expression of  $p(\mathbf{z}_t|\Sigma, \hat{\boldsymbol{\eta}}_t)$  and the inverse-Gamma expression of  $q(\Sigma|\mathbf{r}_{0:t-1})$  and  $q(\Sigma|\mathbf{r}_{0:t})$ , one readily shows that Eq. (21) at iteration  $(\ell) \rightarrow (\ell + 1)$  is given as,

$$\mathcal{E}_2^{(\ell)} \approx \text{cte} + \frac{\hat{\alpha}_t}{\hat{\beta}_t^{(\ell+1)}} \left[ \hat{\beta}_t^{(\ell+1)} - \hat{\beta}_{t-1} - \|\mathbf{z}_t - \mathbf{M}\hat{\boldsymbol{\eta}}_t\|^2/2 \right] - \ln(\hat{\beta}_t^{(\ell+1)}), \quad (22)$$

where cte gathers the terms that do not vary with iterations (i.e., independent of  $(\ell)$ ).

The adaptation of the algorithm above to the case of an inhomogeneous noise with a covariance is straightforward,

$$\Sigma = \text{diag}(\lambda^1, \dots, \lambda^{n_z}), \quad (23)$$

where  $\text{diag}(\mathbf{v})$  denotes a diagonal matrix with diagonal  $\mathbf{v}$ . More specifically, Eqs. (11)-(16) that compute the state ensembles are kept unchanged, and only those related to the noise variance will be updated (i.e., Eqs. (17)-(19) for each  $\lambda^j$ ). Each variance  $\lambda^j$ ,  $j = 1, \dots, n_z$ , is estimated separately from the others,  $\lambda^k$ ,  $k \neq j$ , by a direct application of Eqs. (17)-(19) and (22), which, correspond to the  $n_z \times 1$  vectorial model (3), on the scalar (marginal) model,

$$\mathbf{z}_{t,j} = \mathbf{G}(j, :)\mathbf{x}_t + \mathbf{L}(j, :)\mathbf{x}_{t-1} + \boldsymbol{\xi}_{t,j}, \quad (24)$$

where  $\mathbf{z}_{t,j}$  and  $\boldsymbol{\xi}_{t,j}$  respectively denote the  $j^{th}$  component of  $\mathbf{z}_t$  and  $\boldsymbol{\xi}_t$  (i.e.,  $\boldsymbol{\xi}_{t,j} \sim \mathcal{N}(\mathbf{0}, \lambda^j)$ ), and  $\mathbf{G}(j, :)$  and  $\mathbf{L}(j, :)$  are the  $j^{th}$  rows of  $\mathbf{G}$  and  $\mathbf{L}$ , respectively. A schematic illustration of this algorithm is presented in Figure 2.

FIGURE 2



## 4. Experimental setup

### 4.1. Data merging

A single product for each water flux term of precipitation (**p**) and evaporation (**e**) is required to close the water balance in the second update step of UWCEnKF. One can use only one data product for each flux components, e.g., only TRMM-3B43 for **p** for the filtering process. However, this may introduce errors because various products are subject to a different rate of uncertainty over different areas. Alternatively, the different data products for each component can be merged into a unique **p** and **e** to better represent the water balance over the globally distributed basins (Sahoo et al., 2011). Here, we merge various datasets of precipitation and evaporation prior to data assimilation. To this end, we follow Sahoo et al. (2011) and merge the data considering their relative error levels w.r.t. non-satellite products. This combination is done in a way that satellite-based products are merged to be used in data assimilation while other products are only applied for the merging objective. For **p**, the average of GPCC and CPC unified gauge over each basin is assumed as the truth and is used to estimate the error level of each satellite-based product, i.e., TRMM-3B43, CMORPH, and GPCP. A similar strategy is applied for evaporation, where ERA-interim and VIC products are used to quantify the error level associated with the data of MOD16 and GLEAM outputs that are based on satellite products (Miralles et al., 2011). It is worth mentioning that a more robust merging process can be achieved by involving ground-based measurements as a reference rather than ERA-interim and VIC. Obtaining and analyzing such an enhanced evaporation dataset from in-situ stations over all tested basins is however very difficult and is out of the scope of this study. Therefore, we use these model outputs to merge satellite-based datasets into a single **e**. Once the references are calculated, we use a multiplicative error model to estimate the offset, scale parameter, and error variance for each data product. These variances are then used to compute the observations weights as,

$$w_i = \frac{1}{\sigma_i^2} / \sum_{k=1}^{n_p} \frac{1}{\sigma_k^2}. \quad (25)$$

For each data product ( $i$ ), using the error variances of that specific product  $\sigma_i^2$  and all products ( $\sigma_k^2$ ) in the same data type (with the total number of  $n_p$ ), weight  $w_i$  can be calculated. Eq. (25) is applied for both precipitation and evaporation to provide merged data with reduced error (Luo et al., 2007; Sahoo et al., 2011). Note that the above approach is applied only to merge the various

data products and to obtain uniform precipitation and evaporation datasets prior to assimilation. The estimated errors (e.g.,  $\sigma_i^2$  in Eq. (25)) are used only for this objective and are not related to the water flux error covariance calculation in the filtering procedure (cf. Section 3.2).

#### 4.2. Data assimilation

To start the assimilation process, the initial ensemble is generated by perturbing the forcing fields. To this end, we use Monte Carlo sampling to perturb the precipitation, shortwave radiation, and temperature field considering a Gaussian multiplicative error of 30% for precipitation, an additive Gaussian error of  $50 \text{ W m}^{-2}$  for the shortwave radiation, and a Gaussian additive error of  $2^\circ \text{C}$  for temperature (Jones et al., 2007). The system state includes top soil, shallow soil, deep soil water, snow, vegetation, surface, and groundwater storages. Except for groundwater and surface storage, all the other components are simulated with two hydrological response units (HRU) of tall, e.g., deep-rooted vegetation and short, e.g., shallow-rooted vegetation. This leads to a state vector of dimension  $(2 \times 5 + 1 + 1) \times 1695$  (corresponding to 1695 grid points over all basins).

All observations, including GRACE TWS, satellite soil moisture data, and water fluxes are assimilated monthly. The monthly increment is then be added to each day of the current month, which guarantees that the update of the monthly mean is identical to the monthly mean of the daily updates. Here, the differences between the predictions and the updated state variables are added as offsets to the state variables at the last day of each month to generate the ensembles for the next month assimilation step (see Eicker et al., 2014, for more details). The observation operator aggregates different water storages at each grid point to update with GRACE TWS and scales the top-layer soil storage by the field capacity value to provide a relative wetness for updating with the soil moisture products of AMSR-E and SMOS (Renzullo et al., 2014).

In addition, observation error covariances for the first update step are required. Full error information about the Stokes' coefficients are used to construct the TWS error covariance matrix. This is done by converting GRACE spherical harmonic error coefficients to TWS error covariances following Khaki et al. (2017c). Since such an information is not available for soil moisture products, we assume their error covariances to be uncorrelated with standard deviations of  $0.04 \text{ m}^3 \text{ m}^{-3}$  for SMOS (as suggested by Leroux et al., 2016) and  $0.05 \text{ m}^3 \text{ m}^{-3}$  for AMSR-E (as suggested by De Jeu et al., 2008). We further apply two common auxiliary techniques of ensemble variance inflation and covariance localization to mitigate for the ensemble spread collapse and rank deficiency (Anderson

et al., 2001; Houtekamer and Mitchell, 2001). These include an ensemble inflation with a coefficient factor of 1.12 and Local Analysis (LA) with a localization length scale of  $5^\circ$  (see Khaki et al., 2017b, for more details).

## 5. Results

The results are discussed in three parts. UWCEnKF implementation is first presented and discussed in Section 5.1.1. The validation of the proposed approach against in-situ groundwater and soil moisture measurements is then presented in Section 5.2. The relevance of the second update step in UWCEnKF and its overall effects on the assimilation system performance is finally analyzed in Section 5.3. UWCEnKF estimates are also compared with the results of WCEnKF and EnKF. UWCEnKF is tested with both constant (*Structure in Eq. (10)*, indicated by UWCEnKF-1) and spatially varying (*Structure in Eq. (23)*, indicated by UWCEnKF-2) error variances for the water balance equation. While UWCEnKF-1 assigns a fixed error variance to water fluxes at all points, different values for individual points are calculated by UWCEnKF-2.

### 5.1. Implementation results

#### 5.1.1. Iteration impacts

We first study the sensitivity of UWCEnKF-1, and UWCEnKF-2 to the iteration procedure. As mentioned, in contrast with WCEnKF, which assumes that these uncertainties are known, UWCEnKF estimates the error covariance through an iteration process. To show how this iteration works, we compare the convergence of UWCEnKF-1 and UWCEnKF-2, based on Eq. (22), in Figure 3. The average evolutions of  $\mathcal{E}_2^{(\ell+1)} - \mathcal{E}_2^{(\ell)}$  (the difference between Eq. (22) in each two successive iterations) from both filters for  $\ell = 0 \cdots 10$  are shown in this figure. After few iterations, generally less than 8, both UWCEnKF-1 and UWCEnKF-2 converge. Faster convergence and lower differences  $\mathcal{E}_2^{(\ell+1)} - \mathcal{E}_2^{(\ell)}$  are also generally achieved by UWCEnKF-2 compared to UWCEnKF-1. It can be seen that after 5 iterations, UWCEnKF-2 decreases to a value below the selected arbitrary threshold of  $\mathcal{E}_2^{(\ell+1)} - \mathcal{E}_2^{(\ell)} = 10mm$ . This is due to the fact that UWCEnKF-2 enables more degree of freedom in the optimization process by using different error variance for each grid point as compared to UWCEnKF-1, which tries to fit a single value for the entire domain.

FIGURE 3

In order to demonstrate the relevance of the UWCEnKF, we compare its results against those of the WCEnKF with various preselected values of error variances. The sensitivity of the WCEnKF to the choice of  $\Sigma$  can be seen in Figures 4. The various implementations of the WCEnKF result in different performances in terms of imbalance and the Root-Mean-Squared Error (RMSE), which is calculated based on the assimilation results and groundwater in-situ measurements over the Murray-Darling Basin. The estimated groundwater time series from the WCEnKF and UWCEnKF are spatially interpolated to the nearest gauge stations. The difference between in-situ and filtered time series are then used to calculate the RMSE.

FIGURE 4

Each circle in Figures 4 refers to the average results of an independent implementation of WCEnKF. It can be seen that the results of this filter largely vary depending on the selection of the error variance. Overall, lower imbalance and RMSE are obtained by assuming 20 to 30  $mm^2$ . UWCEnKF-1 and UWCEnKF-2, on the other hand, achieve better results, shown by the triangle and cross, respectively, in a single implementation. The optimization algorithms used in UWCEnKF cause this independence of the error variance choice. It can also be seen that WCEnKF can achieve comparable results to that of UWCEnKF-1 in few cases. UWCEnKF-2, however, generally leads to the minimum RMSE and imbalance.

#### 5.1.2. Spatial and temporal balance error variance

The performance of the proposed UWCEnKF in estimating water balance error variance and their effects on the imbalance between water fluxes are discussed in this section and is further compared with WCEnKF results. Both spatial and temporal variabilities are examined. Figure 5 shows the temporally averaged error variances assigned to the observations for WCEnKF, as well as those estimated by UWCEnKF-1 and UWCEnKF-2 over the Amazon Basin. It can be seen that UWCEnKF-1 and UWCEnKF-2 estimate different errors at each iteration. The error variance maps in WCEnKF, on the other hand, is fixed to what has been assigned prior to data assimilation. After eight iterations, it is observed that the error estimated by UWCEnKF-1 is closer to the average of UWCEnKF-2 results (34.70  $mm^2$ ), i.e., 41.19  $mm^2$  for UWCEnKF-1 and, in comparison to 68.74  $mm^2$  for WCEnKF. This indicates that both UWCEnKF-1 and UWCEnKF-2 result in uncertainties with close magnitude for water balances and the implemented algorithms

allow for such an adjustment during iteration steps. Furthermore, Figure 5 depicts the spatial variability characteristics of error variances estimated by UWCEnKF-2. This property allows for more flexibility for error adjustment in UWCEnKF-2. These flexibilities in the UWCEnKF filtering method, as illustrated in Figure 6, result in a smaller imbalance.

FIGURE 5

FIGURE 6

The better performances of UWCEnKF-1 and UWCEnKF-2 compared to WCEnKF in minimizing imbalance errors are clear in Figure 6, where each map shows the estimated imbalance corresponding to Figure 5 setups. Figure 6 shows that the iteration algorithm effectively reduces imbalance errors, even after only few iterations (e.g., four). In addition, it can be seen that the applied algorithm in UWCEnKF provides the opportunity for error variances to be adjusted with no supervision as in WCEnKF. UWCEnKF-2, with more flexibility for such adjustment than UWCEnKF-1 (cf. Figure 5), leads to the smaller imbalance, that is  $\sim 6$  mm (absolute average of all values) against  $\sim 13$  mm (on average) for UWCEnKF-1. This larger improvement for UWCEnKF-2 results is achieved by estimating different error variance values over each grid point, and correspondingly applying different rate of adjustments (based on the estimated water balance uncertainty) from the equality constraint to the points.

An example of the abovementioned spatially varying error variance in UWCEnKF-2 can be seen in Figure 7. Figure 7a depicts the average imbalance over Murray-Darling basin after jointly assimilating GRACE TWS and satellite soil moisture in the first analysis step of UWCEnKF. It is worth mentioning that we find larger impacts of GRACE TWS data (approximately 7.5 times for all the basins) on the imbalance between fluxes compared to the satellite soil moisture products, which could be explained by the fact that contrary to the soil moisture assimilation, GRACE data influences all compartments. The temporally averaged estimated variances are displayed in Figure 7b. It can be seen that both estimated maps exhibit similar spatial patterns in some areas. One can also see in Figure 7b that, in general, a larger variance is estimated over the areas with larger imbalance. Figure 7c shows the average applied increments in the second analysis step of UWCEnKF-2 to account for the above imbalances. It is clear that larger increments are applied over the areas with larger imbalances, e.g., the north, southeast, and southwest parts of the basin.

The areas such as the central parts, which display smaller imbalance in Figure 7a, are also assigned smaller increments as shown in Figure 7c.

FIGURE 7

Similar flexibilities for error variance estimation in UWCEnKF can also be seen from the temporal variabilities of error variances as demonstrated in Figure 8. The water balance error variances at each assimilation step are estimated from UWCEnKF-1 for the entire Orange Basin and from UWCEnKF-2 for each grid point (green shaded area) of the basin. The figure also plots that of UWCEnKF-2 derived spatially averaged values, as well as errors used in WCEnKF. Again, it is clear from Figure 8 that UWCEnKF-1 and UWCEnKF-2 allow for larger variations in error estimations than WCEnKF. It can also be seen that errors at each point can vary independently in UWCEnKF-2, which results in a better uncertainty adjustment. This can help for optimal imbalance minimization in the filter.

FIGURE 8

FIGURE 9

Both spatial and temporal variabilities of error variances are summarized in Figure 9 over all basins, which shows variation ranges of water balance covariance in time (vertical lines) and space (horizontal lines) for WCEnKF, UWCEnKF-1, and UWCEnKF-2. In contrast to WCEnKF and UWCEnKF-1, spatial variabilities can be observed in UWCEnKF-2 results. As discussed, this helps for a better error adjustment during the filtering process. In terms of temporal variations, both UWCEnKF-1 and UWCEnKF-2 perform comparably well representing a larger range of changes than WCEnKF over all basins. The unsupervised error estimation algorithm in UWCEnKF enables to estimate an “optimal” water balance error calculation, which as it will be shown in Section 5.3 (cf. Figure 15) leads to smaller imbalance errors. In cases where assigned error to WCEnKF is close to what is calculated by UWCEnKF, e.g., Indus Basin, the final achieved imbalance from the filters are also close. In other cases with larger differences between assigned and estimated errors, there are larger discrepancies in imbalances.



## 5.2. *Validations with in-situ measurements*

The performances of the EnKF and UWCEEnKF are compared with in-situ measurements. UWCEEnKF was tested with both constant (UWCEEnKF-1) and spatially varying (UWCEEnKF-2) error variances for the water balance equation. Figure 10 shows the average groundwater time series over the Mississippi, Murray-Darling and the St. Lawrence basins, estimated by the open-loop run (without assimilation), EnKF, WCEEnKF, UWCEEnKF-1, and UWCEEnKF-2. Remarkable improvement can be seen from the different filters compared to the open-loop time series. In this regard, WCEEnKF and UWCEEnKF generally perform better than EnKF. This is more evident when a considerable trend exists in the time series, e.g., within the Murray-Darling basin after 2009 and St. Lawrence between 2010 and 2012. It can also be seen that UWCEEnKF groundwater time series in most of the times better match to those of in-situs. A clear example of this can be found in Murray-Darling basin 2011–2013. Furthermore, comparing UWCEEnKF-1 and UWCEEnKF-2, better agreements between in-situ and estimated groundwater changes are achieved for UWCEEnKF-2 over all three basins, particularly in the Mississippi basin.

FIGURE 10

To better monitor how UWCEEnKF improves the groundwater estimates, their results are compared with in-situ measurements and against those of EnKF. RMSE and standard deviation (STD) are calculated for groundwater error time series, i.e., the difference between in-situ and filtered groundwater time series, at the location of each in-situ station. Figures 11 and 12 display the results over the Murray-Darling and Mississippi basins, respectively.

FIGURE 11

FIGURE 12

One can see that the filters successfully reduce RMSE and STD w.r.t. the open-loop run. This indicates the relevance of assimilation for decreasing state estimate errors. The groundwater estimate improvements are different for each filter. UWCEEnKF-1 and UWCEEnKF-2 suggest more (18% on average) error reduction than EnKF. Overall, more pronounced error reductions are achieved over the Mississippi basins, which could be attributed to larger model errors within the

basin. Slightly better performances ( $\sim 4\%$ ) in terms of groundwater error reduction are obtained with UWCEnKF-2 compared to UWCEnKF-1. We also compute the correlations (at 0.05 significance level) between the filtered and in-situ groundwater time series. Similarly, larger correlations result from the filter estimates compared to the open-loop run, namely, 14% from EnKF, 26% for UWCEnKF-1, and 29% for UWCEnKF-2. The correlation results also confirm that UWCEnKF provides better estimates of the groundwater time series.

In-situ soil moisture measurements are also used to assess the assimilation impact on soil storage. To this end, similar to groundwater assessment, filtered soil moisture time series at the stations' locations are compared with their in-situ counterpoints at different layers. Figure 13 shows root-zone soil moisture variation time series as estimated by the various filters, as well as in-situ measurements over the Mississippi, Murray-Darling, St. Lawrence, Danube, and the Yangtze basins. It can be seen that all filters decrease the misfits between estimated and measured soil moisture variations. In some cases, however, UWCEnKF, and to a lesser degree WCEnKF, performs better, e.g., Mississippi (2009), Murray-Darling (2004 and 2008), and Danube (2006). There are also various occasions during which the WCEnKF and UWCEnKF-1 results are very close, such as St. Lawrence 2010–2012 and Yangtze 2005–2006. This can be explained by the fact that both methods use a single error variance value for water balance uncertainties, so whenever a good approximation is used to assign this value prior to data assimilation in WCEnKF, close to what is estimated in UWCEnKF-1, the corresponding state estimates seen to be also close. UWCEnKF-2, on the other hand, performs relatively better, being more successful in matching soil moisture estimates to the in-situ soil moisture variations.

FIGURE 13

The correlation results between the monthly soil moisture estimates for all filters w.r.t. the monthly in-situ measurements are presented in Table 2. Note that different soil moisture estimates of various soil layers are compared to soil moisture measurements at corresponding layers and their average are reported in the table. For instance, the model top layer is compared with 0-8 cm measurements over the Murray-Darling basin and 0-10 cm over Mississippi basin, summations of the model top, shallow, and a small portion of deep-root soil layers are tested against 0-30 cm and 0-50 cm measurements over the Murray-Darling and Mississippi basins, respectively, and

summations of the model’s soil layers are compared to 0-90 cm (for Murray-Darling) and 0-100 cm (for Mississippi) soil measurements. Due to a difference between the soil moisture estimates (i.e., column water storage measured in mm) and the in-situ measurements (i.e., volumetric soil moisture), only a correlation analysis is conducted. Additionally, in order to statistically assess the results, a significance test for the correlation coefficients is applied based on the t-distribution. The estimated t-value and the distribution at 0.05 significant level are used to calculate the p-value, which is assumed to be significant if it lies under 5%.

TABLE 2

The results indicate that assimilation significantly improves soil storages regardless of the applied filter. All the filters have positive effects on soil moisture estimates. UWCEnKF performs better than both WCEnKF and EnKF with respectively 6% and 11% higher correlations with the in-situ measurements. It can also be seen that in some cases, e.g., Mississippi basin, the filters generally perform comparably, especially WCEnKF and UWCEnKF-1. This indicates that WCEnKF is capable of improving soil moisture estimates as UWCEnKF subject to using an accurate water balance uncertainty because this is the only difference between the two approaches. The largest improvement with an average 20.28% for all basins is achieved by UWCEnKF-2, better than UWCEnKF-1 (17.75% on average) and noticeably larger than EnKF (7.85%).

We further examine the assimilation results against independent discharge data over different basins. It is worth mentioning that these discharge datasets are not assimilated. The average correlations between the estimated water discharge time series and those from the in-situ data over each basin are presented in Table 3. Improvements are achieved for all assimilation experiments w.r.t. the open-loop run. The EnKF increases the correlation by 4% (on average), while UWCEnKF-1 and UWCEnKF-2 increase the correlation by approximately 23% and 24%, respectively. Again, UWCEnKF provides better results than EnKF over all basins. The largest correlation values are obtained for the Murray-Darling and Amazon basins, while the largest correlation improvements are achieved over the Orange, Amazon, and the Yangtze basins.

TABLE 3

### 5.3. Impact of the equality constraint

To further investigate the relevance of the second analysis step of UWCEnKF, we calculate correlations between the filters estimates and assimilated observations at the forecast and analysis steps for all basins. The average correlations improvements w.r.t. the open-loop run are plotted in Figure 14. As expected, larger correlations are obtained in the analysis step. In general, applying EnKF results in larger correlations between the estimates and assimilated observations (e.g., GRACE TWS and AMSR-E+SMOS) because during the EnKF assimilation the full magnitude of the update is applied to the variables regardless of the water balance. However, the WCEnKF and UWCEnKF take into account the water balance in a second update, which leads to the most improvements regarding  $\mathbf{p}$ ,  $\mathbf{e}$ , and  $\mathbf{q}$ . This is due to the fact that the first update in the WCEnKF and UWCEnKF corrects the state variables with the observations, and the second update corrects the water balance. This suggests that water budget constraint slightly degrades the effects of observations in the (second) update step in both WCEnKF and UWCEnKF filters, which is generally due to the observation overfitting problem, when no constraint is applied (e.g., standard EnKF) in data assimilation (see also Tangdamrongsub et al., 2017; Khaki et al., 2017a). Furthermore, there is a degree of disagreement between TWS changes and other flux observations (e.g., precipitation, evaporation, and discharge), which could be attributed to different sources of uncertainties in the observations (see, e.g., Aires, 2014; Munier et al., 2015). The water budget constraint applied to data assimilation (i.e., the second update of UWCEnKF) accounts for this effect by further correcting the estimated states from the first update step based on GRACE TWS. The second step partly removes the artifacts from data assimilation of GRACE in the first step. It can clearly be seen that UWCEnKF provides higher correlations to the flux observations than WCEnKF. This improvement is more pronounced by using UWCEnKF-2. UWCEnKF's both variants remarkably increase the correlations between TWS estimates and water fluxes compared to EnKF. Overall, a better performance is observed for UWCEnKF-2 in comparison to UWCEnKF-1.

FIGURE 14

The results of water budget closure resulting from each filter for every basin are shown in Figure 15. UWCEnKF-1 and UWCEnKF-2 clearly reduce water budget imbalances for all basins compared to WCEnKF and especially EnKF. It can also be seen that UWCEnKF-2 better enforces the balance

between water components after assimilation. The absolute imbalance from UWCEnKF-2 is 15.28 mm, 8.26% smaller than UWCEnKF-1, 17.84% smaller than WCEnKF, and 36.47% smaller than EnKF. Note that these average values are computed for all basins. The imbalance reductions can also be seen from the reported STD values for each time series in Figure 15. In all basins, the largest STD results from the EnKF and the least from the UWCEnKF-2. In some cases such as Indus, and to a lesser degree Amazon, WCEnKF performs comparably to UWCEnKF-1. UWCEnKF-2, on the other hand, achieves the largest water budget imbalance reduction, in terms of amplitude and STD, which confirms the results of Figure 14, as well as the validation results against in-situ measurements.

FIGURE 15

## 6. Conclusions

This study introduced an Unsupervised Weak Constrained Ensemble Kalman Filter (UWCEnKF) to mitigate for water budget imbalance while accounting for uncertainties in the inputs of the water balance components. UWCEnKF is an extension of the previously proposed Weak Constrained Ensemble Kalman Filter (WCEnKF) to a more general (unsupervised) framework, in which the covariance associated with the water balance model is estimated along with the system state. Numerical experiments were carried out to assess the performance of the UWCEnKF against WCEnKF, as well as the standard Ensemble Kalman Filter (EnKF). The filters' results examinations against available in-situ measurements indicated that UWCEnKF performs best in terms of groundwater error reduction and soil moisture estimate improvements. In general, UWCEnKF reduced groundwater errors (w.r.t. groundwater in-situ measurements) by 18% (on average), and 11% (on average) more than EnKF and WCEnKF, respectively. UWCEnKF-2 also achieved 4% (on average) smaller groundwater RMSE than UWCEnKF-1. Furthermore, UWCEnKF increased the correlation values between soil moisture estimates and those of the in-situ measurements by 6% more than WCEnKF and 12% more than EnKF. Again, UWCEnKF-2 performed better than UWCEnKF-1 with larger soil moisture correlations w.r.t. the in-situ soil moisture measurements, i.e., 20.28% against 17.75%. UWCEnKF also achieved larger correlations to independent discharge datasets, e.g., respectively 6% and 11% larger correlations with the in-situ measurements than WCEnKF and EnKF. The experiments results also suggested that the UWCEnKF using spatially

varying error variances for the water balance equation provides better groundwater and soil moisture estimates than applying a constant error variance. A similar performance was also obtained for the water budget imbalance reduction, where the prior variant better mitigated the imbalance problem than the latter case.

Overall, UWCEnKF achieved maximum correlations with the flux observations, both during the forecast and analysis steps. The largest imbalance reduction was also obtained using UWCEnKF. More specifically, the absolute imbalance for UWCEnKF-2 is 15.28 mm, 8.26% smaller than UWCEnKF-1, 17.84% smaller than WCEnKF, and 36.47% smaller than EnKF. These results demonstrate the relevance of the new proposed unsupervised scheme, which is straightforward to implement and computationally not intensive. Future work will consider extending the proposed framework to jointly estimate the model biases with the state and the observation error variance.

## Acknowledgement

M. Khaki is grateful for the research grant of Curtin International Postgraduate Research Scholarships (CIPRS)/ORD Scholarship provided by Curtin University (Australia). This work is a TIGeR publication.

## References

- Adler, R.F., Susskind, J., Huffman, G.J., Bolvin, D., Nelkin, E., Chang, A., et al., (2003). Global precipitation climatology project V2.1 monthly 2.5 deg global 1979present (satellite only and gauge adjusted) 2003: The version-2 global precipitation climatology project (GPCP) monthly precipitation analysis (1979present). *Journal of Hydrometeorology*, 4, 1147-1167.
- Ait-El-Fquih, B., Hoteit, I., (2015). Fast Kalman-like Filtering in large-dimensional linear and Gaussian state-space models. *IEEE Transactions on Signal Processing*, 63, 5853–5867.
- Ait-El-Fquih, B., Hoteit, I., (2016). A variational Bayesian multiple particle filtering scheme for large-dimensional systems. *IEEE Transactions on Signal Processing*, 64, 5409–5422.
- Anderson, J., (2001). An Ensemble Adjustment Kalman Filter for Data Assimilation. *Mon. Wea. Rev.*, 129, 2884-2903, [http://dx.doi.org/10.1175/1520-0493\(2001\)129;2884:AEAKFF;2.0.CO;2](http://dx.doi.org/10.1175/1520-0493(2001)129;2884:AEAKFF;2.0.CO;2).



638 Aires, F., (2014). Combining datasets of satellite retrieved products. Part I: Methodology and water  
639 budget closure. *Journal of Hydrometeorology*, 15 (4), 1677-1691.

640 Blei, David M., Alp Kucukelbir, and Jon D. McAuliffe (2017). Variational Inference: A Re-  
641 view for Statisticians. *Journal of the American Statistical Association*, 112:518, 859–877, DOI:  
642 10.1080/01621459.2017.1285773.

643 Chen, M., Xie, P., Janowiak, J.E., Arkin, P.A., (2002). Global land precipitation: A 50-yr monthly  
644 analysis based on gauge observations. *Journal of Hydrometeorology*, 3, 249-266.

645 Cheng, M.K., Tapley, B.D., (2004). Variations in the Earth’s oblateness during  
646 the past 28 years. *Journal of Geophysical Research, Solid Earth*, 109, B09402.  
647 <http://dx.doi.org/10.1029/2004JB003028>.

648 De Jeu, R.A.M., Owe, M., (2003). Further validation of a new methodology for sur-  
649 face moisture and vegetation optical depth retrieval. *Int J Remote Sens* 24:4559-4578,  
650 <http://dx.doi.org/10.1080/0143116031000095934>.

651 De Jeu, R.A.M., Wagner, W., Holmes, T.R.H., Dolman, A.J., van de Giesen, N.C.,  
652 Friesen J., (2008) Global Soil Moisture Patterns Observed by Space Borne Microwave Ra-  
653 diometers and Scatterometers, *Surveys in Geophysics*, Volume 29, Issue 45, pp 399-420,  
654 <http://dx.doi.org/10.1007/s10712-008-9044-0>.

655 Doll, P., Kaspar, F., Lehner, B., (2003). A global hydrological model for deriving water availability  
656 indicators: model tuning and validation, *J. Hydrol.*, 270, 105-134.

657 Draper, C.S., Mahfouf, J.-F., Walker, J.P., (2009), An EKF assimilation of AMSR-  
658 E soil moisture into the ISBA land surface scheme, *J. Geophys. Res.*, 114, D20104,  
659 <http://dx.doi.org/10.1029/2008JD011650>.

660 Drusch, M., Wood, E.F., Gao, H., (2005). Observation operators for the direct assimilation of  
661 TRMM microwave imager retrieved soil moisture. *Geophysical Research Letters*, 32, L15403.

662 Eicker, A., Schumacher, M., Kusche, J., Dll, P., Mller-Schmied, H., (2014). Calibration/data  
663 assimilation approach for integrating GRACE data into the WaterGAP global hydrology  
664 model (WGHM) using an ensemble Kalman filter: first results, *Surv Geophys*, 35(6):1285-1309.  
665 <http://dx.doi.org/10.1007/s10712-014-9309-8>.

666 Gutentag, E.D., Heimes, F.J., Krothe, N.C., Luckey, R.R., Weeks, J.B., (1984). Geohydrology of  
667 the High Plains aquifer in parts of Colorado, Kansas, Nebraska, New Mexico, Oklahoma, South  
668 Dakota, Texas, and Wyoming, U.S. Geol. Surv. Prof. Pap., 1400-B, 66 pp.

669 Han, R., Tian, X.J., Fu, Y., Cai, Z.N., (2015). Real-data assimilation experiment with a joint  
670 data assimilation system: assimilating carbon dioxide mole fraction measurements from the  
671 Greenhouse gases Observing Satellite, Atmospheric and Oceanic Science Letters, Volume 9, Issue  
672 2, Pages 107-113, <https://doi.org/10.1080/16742834.2016.1133070>.

673 Houtekamer, P.L., Mitchell, H.L., (2001). A Sequential Ensemble Kalman Filter for Atmospheric  
674 Data Assimilation, Mon. Wea. Rev., 129:1, 123-137.

675 Huffman, G.J., Adler, R.F., Bolvin, D.T., Gu, G., Nelkin, E.J., Bowman, K.P., Hong, Y., Stocker,  
676 E.F., Wolff, D.B., (2007). The TRMM Multi-satellite Precipitation Analysis: Quasi- Global,  
677 Multi-Year, Combined-Sensor Precipitation Estimates at Fine Scale. J. Hydrometeor., 8(1), 38-  
678 55.

679 Jaakkola, T.S., Jordan, M.I., (2000). Bayesian parameter estimation via variational methods. Statis-  
680 tics and Computing, 10, 25-37.

681 Jackson, T., Bindlish, R., (2012). Validation of Soil Moisture And Ocean Salinity (SMOS) soil  
682 moisture over watershed networks in the US, IEEE Trans. Geosci. Remote Sens., 50, 15301543.

683 Jones, D.A., Wang, W., Fawcett, R., Grant, I., (2007). Climate data for the Australian water  
684 availability project. In: Australian Water Availability Project Milestone Report. Bur. Met.,  
685 Australia, 37pp.

686 Joyce, R.J., Janowiak, J.E., Arkin, P.A., Xie, P.P., (2004). CMORPH: A method that produces  
687 global precipitation estimates from passive microwave and infrared data at high spatial and  
688 temporal resolution. Journal of Hydrometeorology, 5, 487503.

689 Khaki, M., Ait-El-Fquih, B., Hoteit, I., Forootan, E., Awange, J., Kuhn, M., (2017a). A  
690 Two-update Ensemble Kalman Filter for Land Hydrological Data Assimilation with an Un-  
691 certain Constraint, Journal of Hydrology, Volume 555, Pages 447-462, ISSN 0022-1694,  
692 <https://doi.org/10.1016/j.jhydrol.2017.10.032>.

- 693 Khaki, M., Schumacher, M., J., Forootan, Kuhn, M., Awange, E., van Dijk, A.I.J.M., (2017b). Ac-  
694 counting for Spatial Correlation Errors in the Assimilation of GRACE into Hydrological Models  
695 through localization, *Advances in Water Resources*, Volume 108, Pages 99-112, ISSN 0309-1708,  
696 <https://doi.org/10.1016/j.advwatres.2017.07.024>.
- 697 Khaki, M., Hoteit, I., Kuhn, M., Awange, J., Forootan, E., van Dijk, A.I.J.M., Schumacher, M., Pat-  
698 tiaratchi, C., (2017c). Assessing sequential data assimilation techniques for integrating GRACE  
699 data into a hydrological model, *Advances in Water Resources*, Volume 107, Pages 301-316, ISSN  
700 0309-1708, <http://dx.doi.org/10.1016/j.advwatres.2017.07.001>.
- 701 Khaki, M., Forootan, E., Kuhn, M., Awange, J., Papa, F., Shum, C.K., (2018a).  
702 A Study of Bangladesh's Sub-surface Water Storages Using Satellite Products  
703 and Data Assimilation Scheme. *Science of The Total Environment*, 625:963-977,  
704 <https://doi.org/10.1016/j.scitotenv.2017.12.289>.
- 705 Khaki, M., Forootan, E., Kuhn, M., Awange, J., van Dijk, A.I.J.M., Schumacher, M.,  
706 Sharifi, M.A., (2018b). Determining Water Storage Depletion within Iran by Assimilating  
707 GRACE data into the W3RA Hydrological Model. *Advances in Water Resources*, 114:1-18,  
708 <https://doi.org/10.1016/j.advwatres.2018.02.008>.
- 709 Khaki, M., Forootan, E., Kuhn, M., Awange, J., Longuevergne, L., Wada, W., (2018c). Efficient  
710 Basin Scale Filtering of GRACE Satellite Products, *Remote Sensing of Environment*, Volume  
711 204, Pages 76-93, ISSN 0034-4257, <https://doi.org/10.1016/j.rse.2017.10.040>.
- 712 Kusche, J., Schmidt R., Petrovic, S., Rietbroek, R., (2009). Decorrelated GRACE time-variable  
713 gravity solutions by GFZ and their validation using a hydrological model, *Journal of Geodesy*,  
714 <http://dx.doi.org/10.1007/s00190-009-0308-3>.
- 715 Leroux, D.J., Pellarin, T., Vischel, T., Cohard, J.-M., Gascon, T., Gibon, F., Mialon, A., Galle, S.,  
716 Peugeot, C., Seguis, L., (2016). Assimilation of SMOS soil moisture into a distributed hydrological  
717 model and impacts on the water cycle variables over the Oum catchment in Benin, *Hydrol. Earth  
718 Syst. Sci.*, 20, 2827-2840, <https://doi.org/10.5194/hess-20-2827-2016>.
- 719 Liang, X., Lettenmiar, D.P., Wood, E.F., Burges, S.J., (1994). A simple hydrologically based model  
720 of landsurfacewater and energy fluxes for general-circulationmodels. *Journal of Geophysical Re-  
721 search*, 99, 14,41514,428. <http://dx.doi.org/10.1029/94JD00483>.

- 722 Lievens, H., Reichle, R.H., Liu, Q., De Lannoy, G.J.M., Dunbar, R.S., Kim, S.B.,  
723 Das, N.N., Cosh, M., Walker, J.P., Wagner, W., (2017). Joint Sentinel-1 and SMAP  
724 data assimilation to improve soil moisture estimates, *Geophys. Res. Lett.*, 44, 61456153,  
725 <https://doi.org/10.1002/2017GL073904>.
- 726 Liu, C., Xue, M., (2016). Relationships among Four-Dimensional Hybrid Ensemble Variational Data  
727 Assimilation Algorithms with Full and Approximate Ensemble Covariance Localization. *Mon.*  
728 *Wea. Rev.*, 144, 591606, <http://dx.doi.org/10.1175/MWR-D-15-0203.1>.
- 729 Luo, L., Wood, E.F., Pan, M., (2007). Bayesian merging of multiple climate model fore-  
730 casts for seasonal hydrological predictions. *Journal of Geophysical Research*, 112, D10102.  
731 <http://dx.doi.org/10.1029/2006JD007655>.
- 732 Massoud, E. C., Huisman, J. , Beninc, E. , Dietze, M. C., Bouten, W. , Vrugt, J. A., Adler, F.,  
733 (2018). Probing the limits of predictability: data assimilation of chaotic dynamics in complex  
734 food webs. *Ecol Lett*, 21: 93-103, <http://dx.doi.org/10.1111/ele.12876>.
- 735 Mayer-Gürr, T., Zehentner, N., Klinger, B., Kvas, A., (2014). ITSG-Grace2014: a new GRACE  
736 gravity field release computed in Graz. - in: GRACE Science Team Meeting (GSTM), Potsdam  
737 am: 29.09.2014.
- 738 Miralles, D.G., Holmes, T.R.H., de Jeu, R.A.M., Gash, J.H., Meesters, A.G.C.A., Dolman, A.J.,  
739 (2011), Global land-surface evaporation estimated from satellite-based observations, *Hydrology*  
740 *and Earth System Sciences*, 15, 453469.
- 741 Mu, Q., Heinsch, F.A., Zhao, M., Running, S.W., (2007). Development of a global evapotranspira-  
742 tion algorithm based on MODIS and global meteorology data. *Remote Sensing of Environment*  
743 111, 519-536, <http://dx.doi.org/10.1016/j.rse.2007.04.015>.
- 744 Munier, S., Aires, F., Schlaffer, S., Prigent, C., Papa, F., et al., (2015). Combining datasets of satel-  
745 lite retrieved products for basin-scale water balance study. Part II: Evaluation on the Mississippi  
746 Basin and closure correction model. *Journal of Geophysical Research: Atmospheres*, American  
747 Geophysical Union, 2014, 119, pp.100-116.
- 748 Njoku, E.G. et al. (2003). Soil moisture retrieval from AMSR-e. *IEEE Transactions on Geo-science*  
749 *and Remote Sensing*. 41:2, 215-229.

750 Njoku, E.G., (2004). AMSR-E/Aqua Daily L3 Surface Soil Moisture, Interpretive Parameters, QC  
751 EASE-Grids. Version 2. [indicate subset used]. Boulder, Colorado USA: NASA National Snow  
752 and Ice Data Center Distributed Active Archive Center. doi: 10.5067/AMSR-E/AE.LAND3.002.

753 Pan, M., Wood, E.F., (2006). Data assimilation for estimating the terrestrial water budget using a  
754 constrained ensemble Kalman filter. *Journal of Hydrometeorology*, 7 (3), 534-547.

755 Pan, M., Sahoo, A.K., Troy, T.J., Vinukollu, R.K., Sheffield, J., Wood, E.F., (2012). Multisource  
756 Estimation of Long-Term Terrestrial Water Budget for Major Global River Basins. *Journal of*  
757 *Climate*, 25 (9), 3191-3206.

758 Reager, J.T., Thomas, A.C., Sproles, E.A., Rodell, M., Beaudoin, H.K., Li, B., Famiglietti, J.S.,  
759 (2015). Assimilation of GRACE Terrestrial Water Storage Observations into a Land Surface  
760 Model for the Assessment of Regional Flood Potential. *Remote Sensing*, 7(11):14663-14679,  
761 doi:10.3390/rs71114663.

762 Reichle, R.H., Koster, R.D., (2004). Bias reduction in short records of satellite soil moisture, *Geo-*  
763 *phys. Res. Lett.*, 31, L19501, <http://dx.doi.org/10.1029/2004GL020938>.

764 Renzullo, L.J., Van Dijk, A.I.J.M., Perraud, J.M., Collins, D., Henderson, B., Jin, H.,  
765 Smith, A.B., McJannet, D.L., (2014). Continental satellite soil moisture data assimilation im-  
766 proves root-zone moisture analysis for water resources assessment. *J. Hydrol.*, 519, 274-276.  
767 <http://dx.doi.org/10.1016/j.jhydrol.2014.08.008>.

768 Rodell, M., Chen, J., Kato, H., Famiglietti, J.S., Nigro, J., Wilson, C.R., (2007). Estimating  
769 groundwater storage changes in the Mississippi River basin (USA) using GRACE, *Hydrogeol. J.*,  
770 15, 159-166.

771 Sahoo, A.K., Pan, M., Troy, T.J., Vinukollu, R.K., Sheffield, J., Wood, E.F., (2011). Reconciling the  
772 global terrestrial water budget using satellite remote sensing. *Remote Sensing of Environment*,  
773 115 (8), 1850-1865.

774 Sato, M., (2001). Online model selection based on the variational Bayes. *Neural Computation*, 13,  
775 1649-1681.

776 Schneider, U., Fuchs, T., Meyer-Christoffer, A., Rudolf, B., (2008). In G. P. C. Centre (Ed.),  
777 Internet publication.

778 Seoane, L., Ramillien, G., Frappart, F., Leblanc, M., (2013). Regional GRACE-based estimates of  
779 water mass variations over Australia: validation and interpretation, *Hydrol. Earth Syst. Sci.*, 17,  
780 4925-4939, <http://dx.doi.org/10.5194/hess-17-4925-2013>.

781 Schumacher, M., Kusche, J., Dll, P., (2016). A systematic impact assessment of GRACE  
782 error correlation on data assimilation in hydrological models, *Journal of Geodesy*,  
783 <http://dx.doi.org/10.1007/s00190-016-0892-y>.

784 Simmons, A. J., Uppala, S., Dee, D., Kobayashi, S., (2007). ERA-interim: New ECMWF reanalysis  
785 products from 1989 onwards, *ECMWF Newsletter No. 110 Winter 2006/07*.

786 Simon, D., Chia, T.L., (2002). Kalman filtering with state equality constraints. *IEEE Trans. Aerosp.*  
787 *Electron. Syst.*, 38, 128136.

788 Smidl, V., Quinn, A., (2006). *The Variational Bayes Method in Signal Processing*. Springer.

789 Smidl, V., Quinn, A., (2008). Variational Bayesian Filtering. *IEEE Transactions on Signal Process-*  
790 *ing*, 56, 5020–5030.

791 Smith, A.B., Walker, J.P., Western, A.W., Young, R.I., Ellett, K.M., Pipunic, R.C., Richter, H.,  
792 (2012). The Murrumbidgee soil moisture monitoring network data set. *Water Resour. Res.* 48  
793 (7), 16. <http://dx.doi.org/10.1029/2012WR011976>.

794 Sokolov, A.A., Chapman, T.G., (1974). *Methods for Water Balance Computation An International*  
795 *Guide for Research and Practice*. The Unesco Press, Paris.

796 Strassberg, G., Scanlon, B.R., Rodell, M., (2007). Comparison of seasonal terrestrial water storage  
797 variations from GRACE with groundwater-level measurements from the High Plains Aquifer  
798 (USA), *Geophys. Res. Lett.*, 34, L14402, <http://dx.doi.org/10.1029/2007GL030139>.

799 Su, C.-H., Ryu, D., Young, R.I., Western, A.W., Wagner, W., (2013). Inter-comparison of mi-  
800 crowave satellite soil moisture retrievals over the Murrumbidgee Basin, southeast Australia. *Re-*  
801 *mote Sensing of Environment*, 134, 111.

802 Swenson, S., Chambers, D., Wahr, J., (2008). Estimating geocentervariations from a combi-  
803 nation of GRACE and ocean model output. *Journal of Geophysical research*, 113, B08410,  
804 <http://dx.doi.org/10.1029/2007JB005338>.



805 Tangdamrongsub, N., Steele-Dunne, S.C., Gunter, B.C., Ditmar, P.G., Sutanudjaja, E.H., Xie,  
806 T, Wang, Z., (2017). Improving estimates of water resources in a semi-arid region by assimila-  
807 ting GRACE data into the PCR-GLOBWB hydrological model, *Hydrology and Earth System*  
808 *Sciences*, 21, 2053-2074.

809 Tian, S., Tregoning, P., Renzullo, L.J., van Dijk, A.I.J.M., Walker, J.P., Pauwels, V.R.N.,  
810 Allgeyer, S., (2017). Improved water balance component estimates through joint assimila-  
811 tion of GRACE water storage and SMOS soil moisture retrievals, *Water Resour. Res.*, 53,  
812 <http://dx.doi.org/10.1002/2016WR019641>.

813 Tregoning, P., McClusky, S., van Dijk, A.I.J.M., Crosbie, R.S., Pea-Arancibia, J.L., (2012). Assess-  
814 ment of GRACE Satellites for Groundwater Estimation in Australia, *National Water Commis-*  
815 *sion*, Canberra, 82 pp.

816 van Dijk, A.I.J.M., (2010). The Australian Water Resources Assessment System: Technical Report  
817 3, Landscape model (version 0.5) Technical Description, CSIRO: Water for a Healthy Country  
818 National Research Flagship.

819 van Dijk, A.I.J.M., Renzullo, L.J., Wada, Y., Tregoning, P., (2014). A global water cycle reanalysis  
820 (20032012) merging satellite gravimetry and altimetry observations with a hydrological multi-  
821 model ensemble. *Hydrol Earth Syst Sci* 18:29552973. [http://dx.doi.org/10.5194/hess-18-2955-](http://dx.doi.org/10.5194/hess-18-2955-2014)  
822 [2014](http://dx.doi.org/10.5194/hess-18-2955-2014).

823 Wahr, J.M., Molenaar, M., Bryan, F., (1998). Time variability of the Earth's gravity field:  
824 hydrological and oceanic effects and their possible detection using GRACE. *J Geophys Res*  
825 108(B12):3020530229, <http://dx.doi.org/10.1029/98JB02844>.

826 Zaitchik, B.F., Rodell, M., Reichle, R.H., (2008). Assimilation of GRACE terrestrial water stor-  
827 age data into a land surface model: results for the Mississippi River Basin. *J Hydrometeorol*  
828 9(3):535548, <http://dx.doi.org/10.1175/2007JHM951.1>.

829 Zhang, J., Campbell, J.R., Hyer, E.J., Reid, J.S., Westphal, D.L., Johnson R.S., (2014). Evaluating  
830 the impact of multisensor data assimilation on a global aerosol particle transport model, *J.*  
831 *Geophys. Res. Atmos.*, 119, 46744689, <http://dx.doi.org/10.1002/2013JD020975>.

832 Zhang, Y., Pan, M., Wood, E.F., (2016). On Creating Global Gridded Terrestrial Water Budget  
833 Estimates from Satellite Remote Sensing. *Surveys in Geophysics*, 37 (2), 249268.

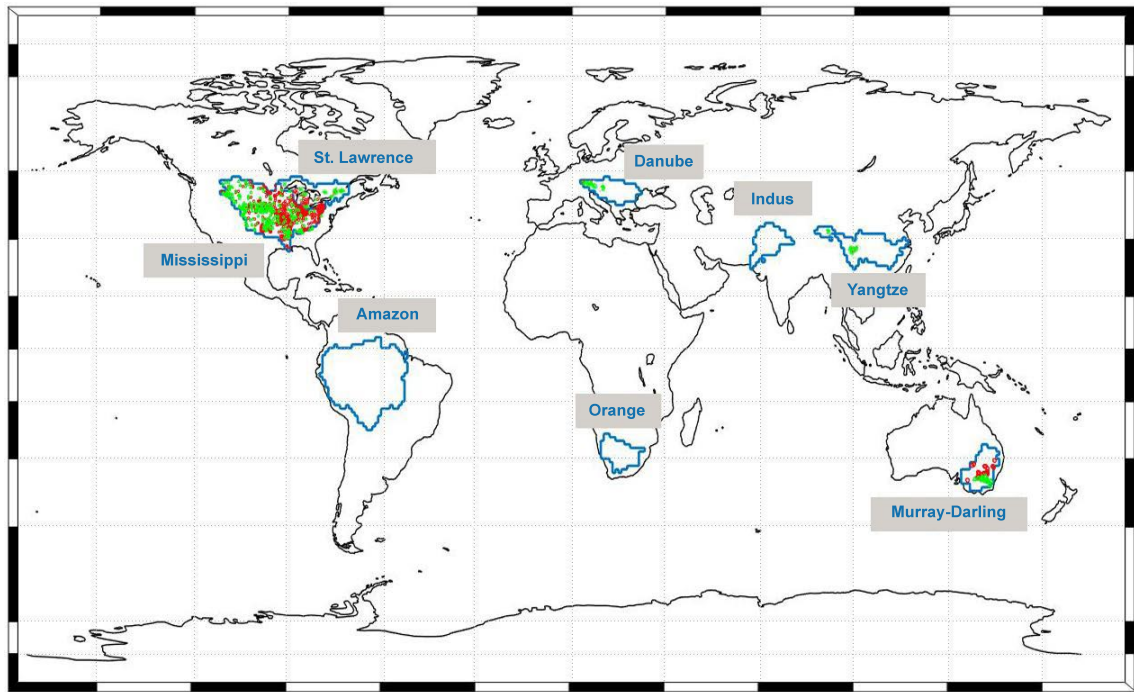


Figure 1: The location of study basins. The figure also contains the distribution of in-situ groundwater (red) and soil moisture (green) gauge stations.

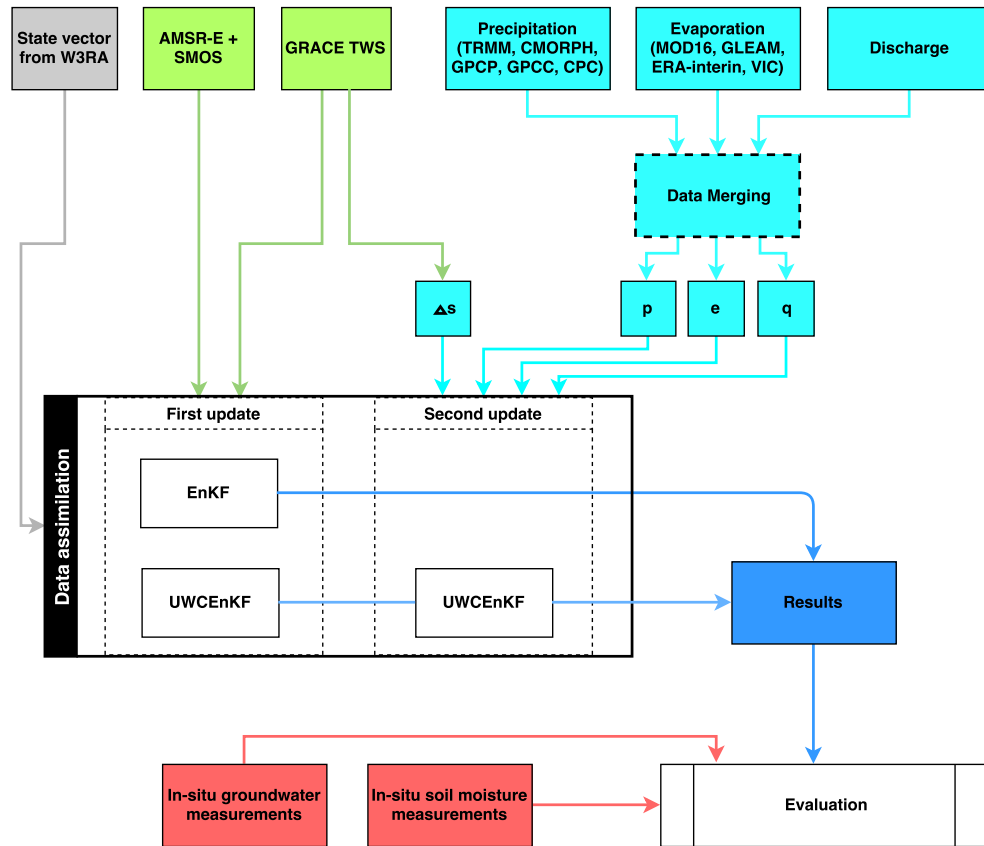


Figure 2: A schematic illustration of the UWCEnKF steps applied for data assimilation, as well as data merging process.

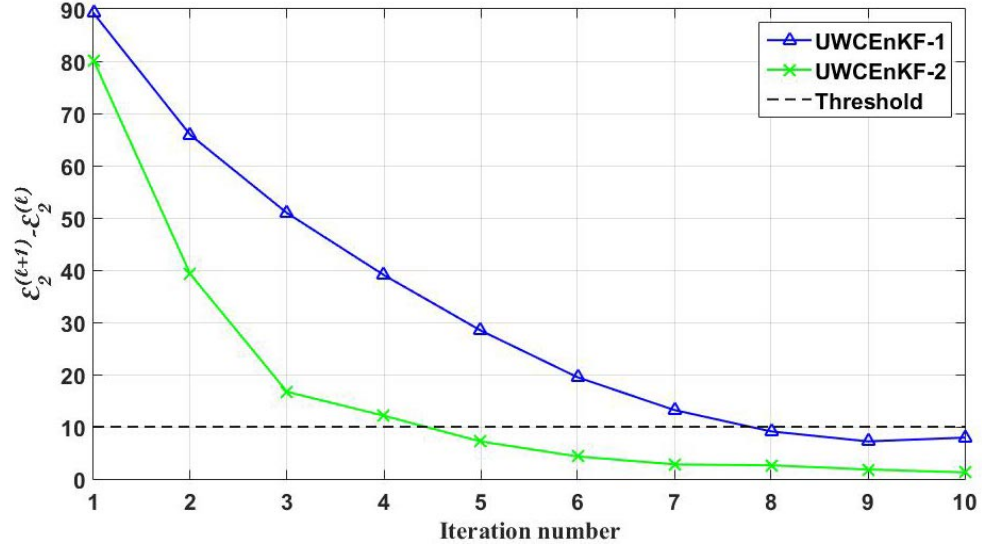


Figure 3: Average  $\mathcal{E}_2^{(\ell+1)} - \mathcal{E}_2^{(\ell)}$  estimates (unit is mm) from UWCEnKF-1 and UWCEnKF-2 filters during assimilation in each iteration (for  $\ell = 0 \cdots 10$ ). The threshold value (10mm) is chosen arbitrary based on a trial and error procedure.

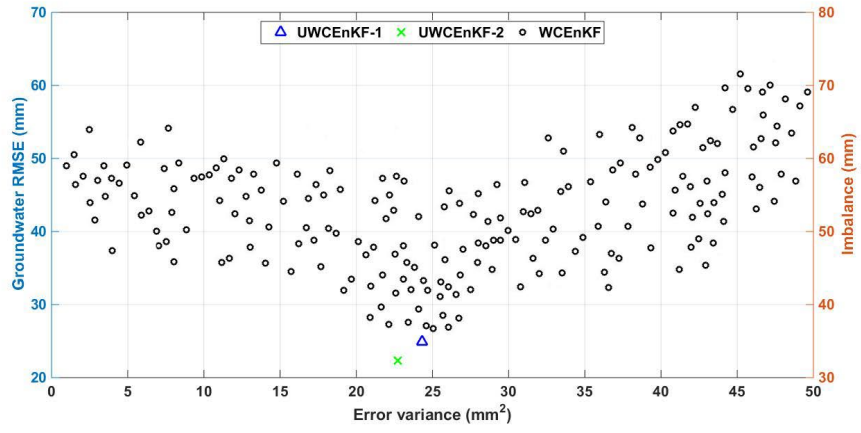


Figure 4: Average groundwater RMSE and imbalance for various implementations of the WCEnKF filter using different error variance assumed (circles) considering different error variance. UWCEnKF-1 and UWCEnKF-2 results are indicated by triangle and cross, respectively.

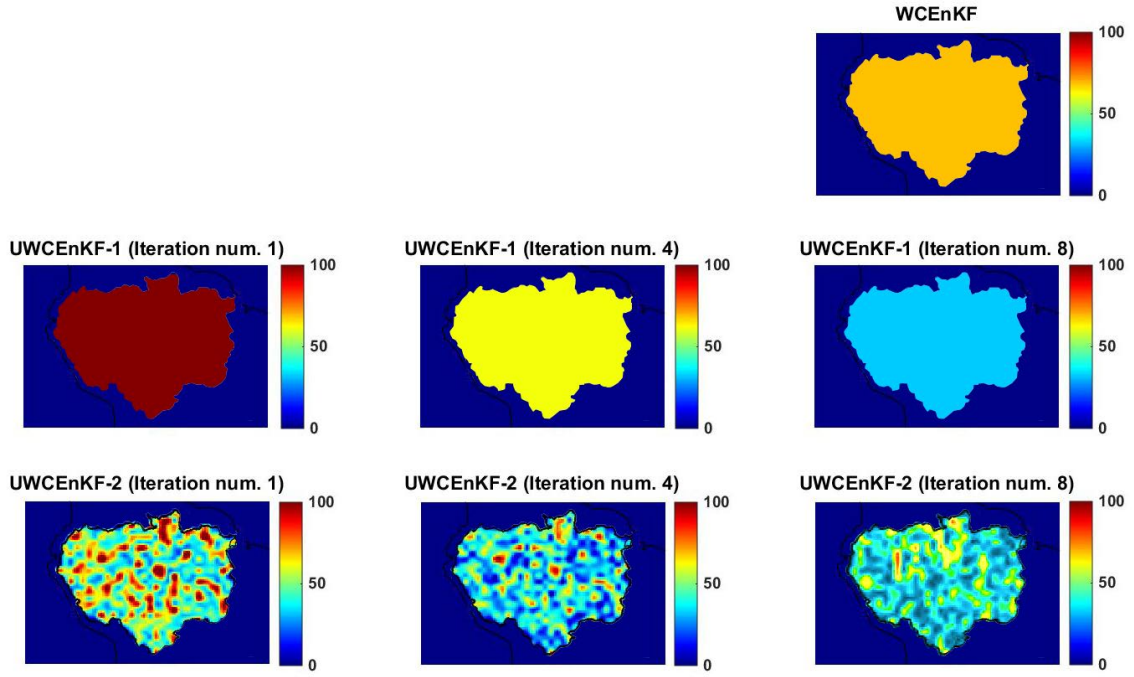


Figure 5: Spatial variability of error variances estimated by WCEEnKF, UWCEEnKF-1, and UWCEEnKF-2. The corresponding results for different iterations are also demonstrated for WCEEnKF-1 and UWCEEnKF-2.

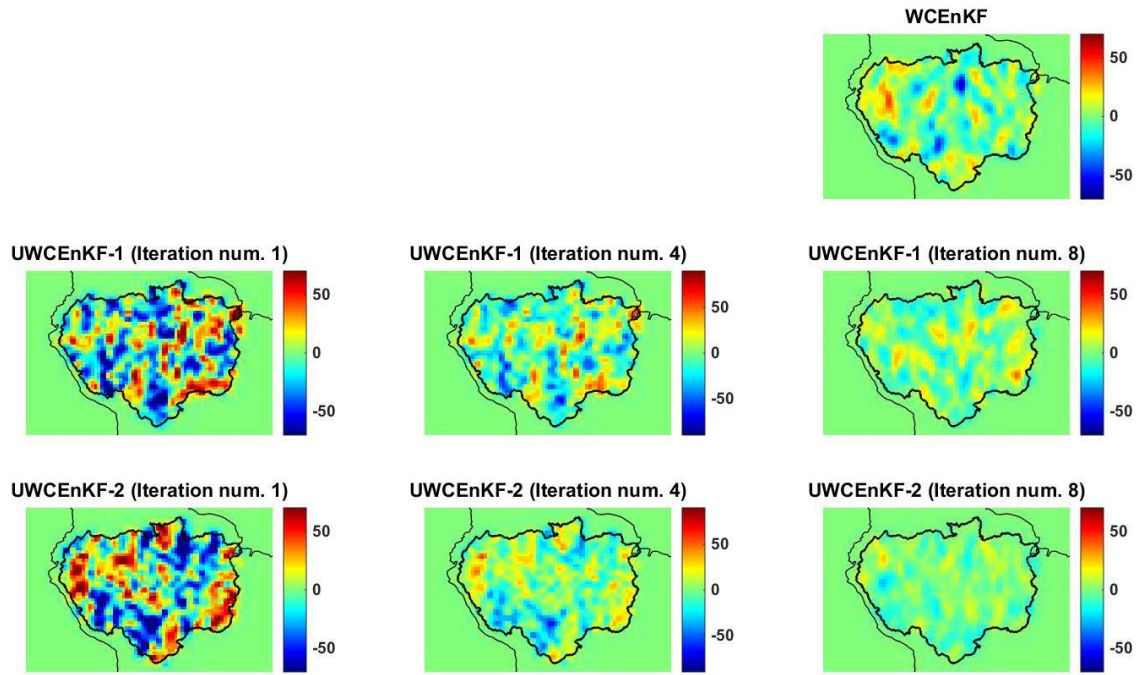


Figure 6: Spatial variability of imbalances from WCEnKF, UWCEnKF-1, and UWCEnKF-2 corresponding to the errors presented in Figure 5.

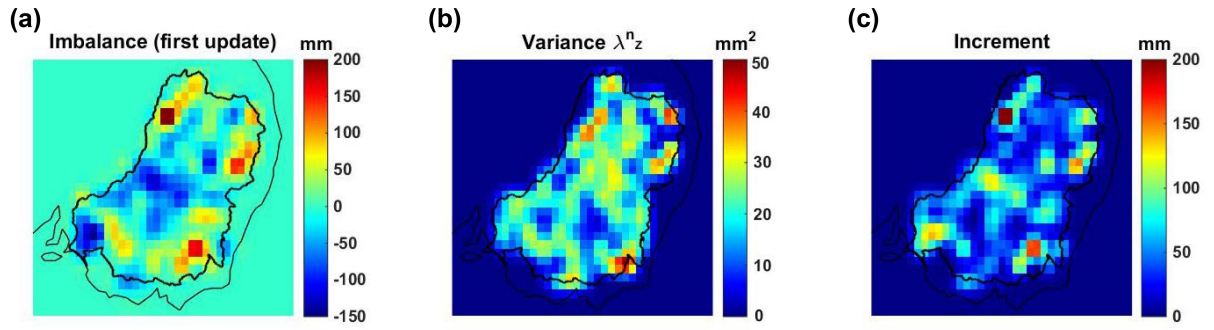


Figure 7: Temporarily averaged maps of imbalances from UWCEnKF-2's first update (a), estimated error variance (b), and increments applied in the second analysis step of UWCEnKF-2 (c).



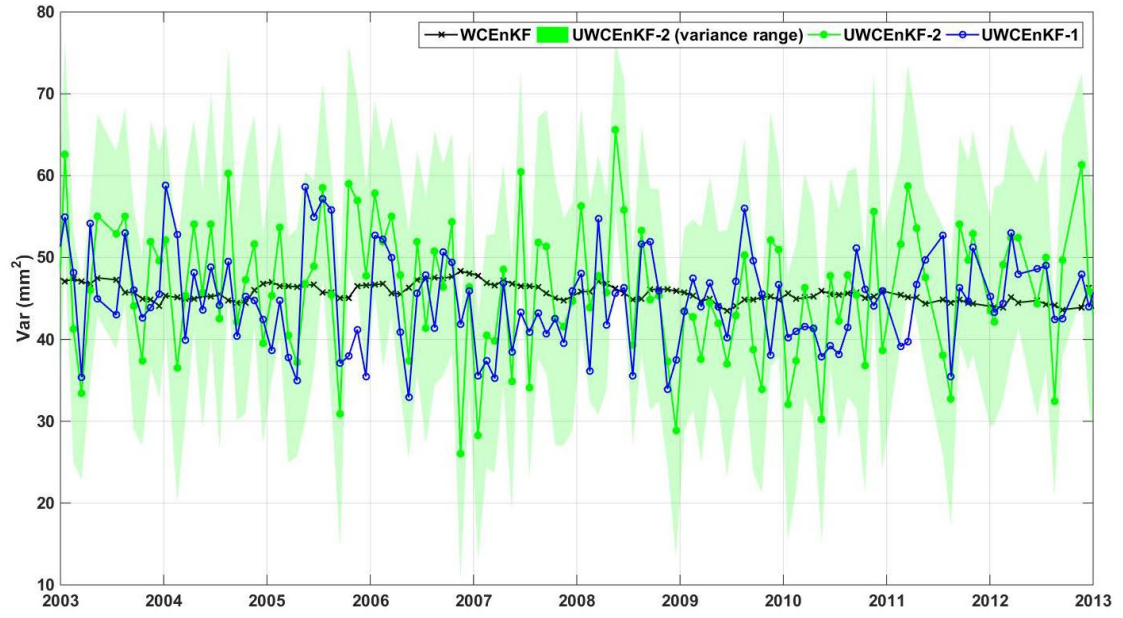


Figure 8: Average water balance variances estimated by UWCEEnKF-1 and UWCEEnKF-2. The plots also contains the assigned variance values for WCEEnKF implementation.

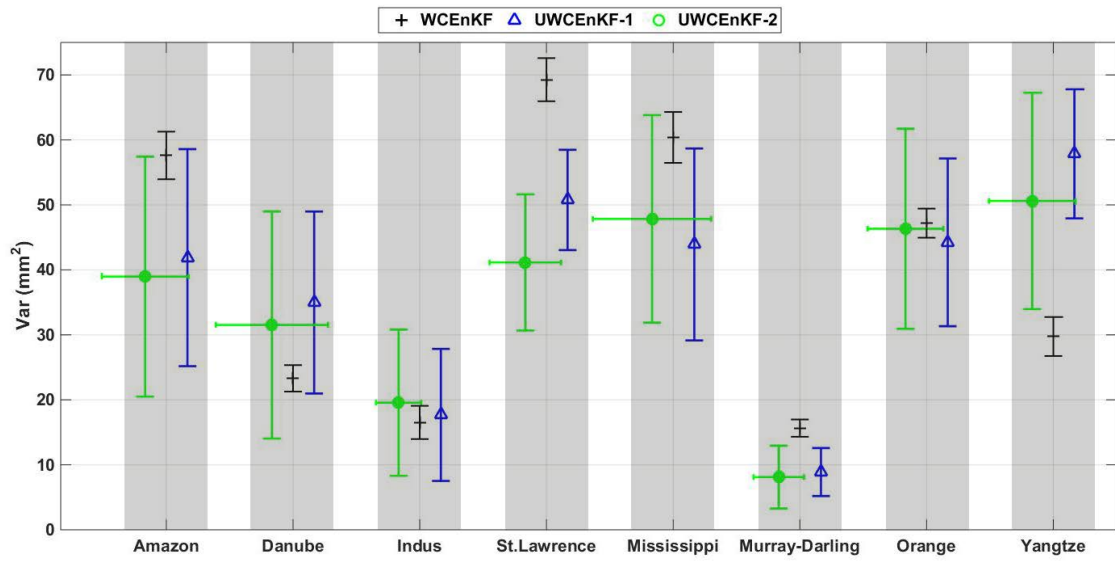


Figure 9: Variation ranges of water balance covariance in time (vertical lines) and space (horizontal lines) for WCEEnKF, UWCEEnKF-1, and UWCEEnKF-2.

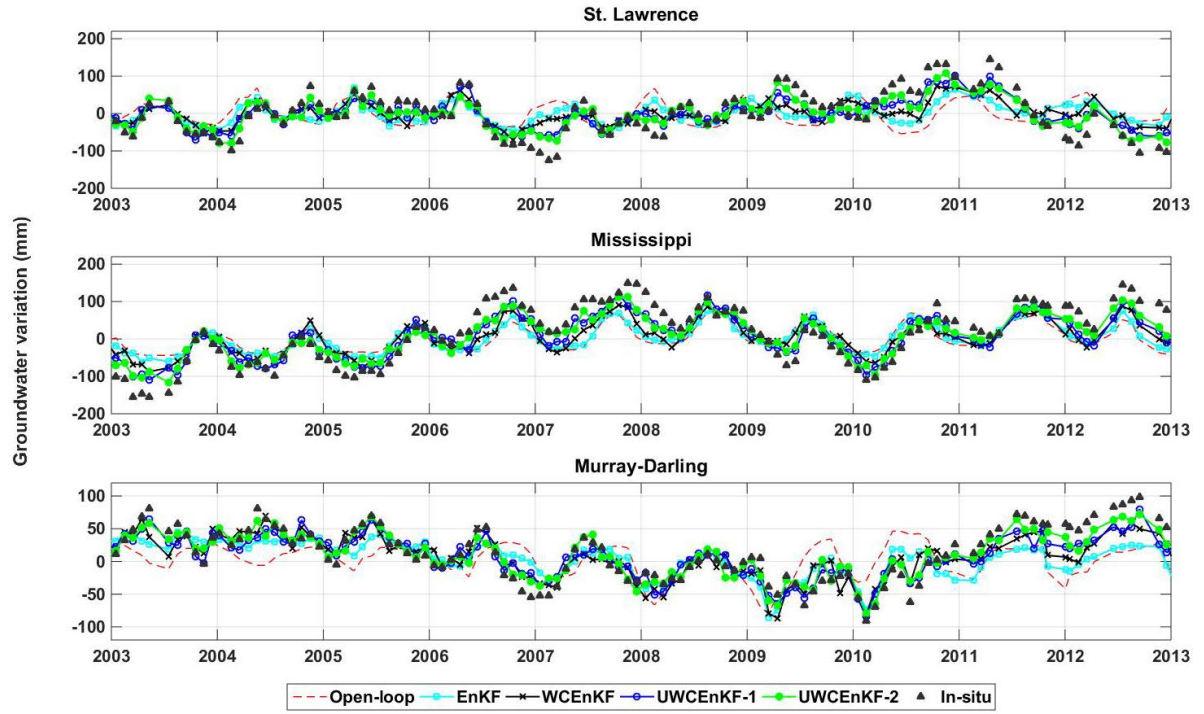


Figure 10: Average groundwater variation time series by the open-loop run, EnKF, WCEEnKF, UWCEEnKF-1, and UWCEEnKF-2 over St. Lawrence, Mississippi, and Murray-Darling basins.

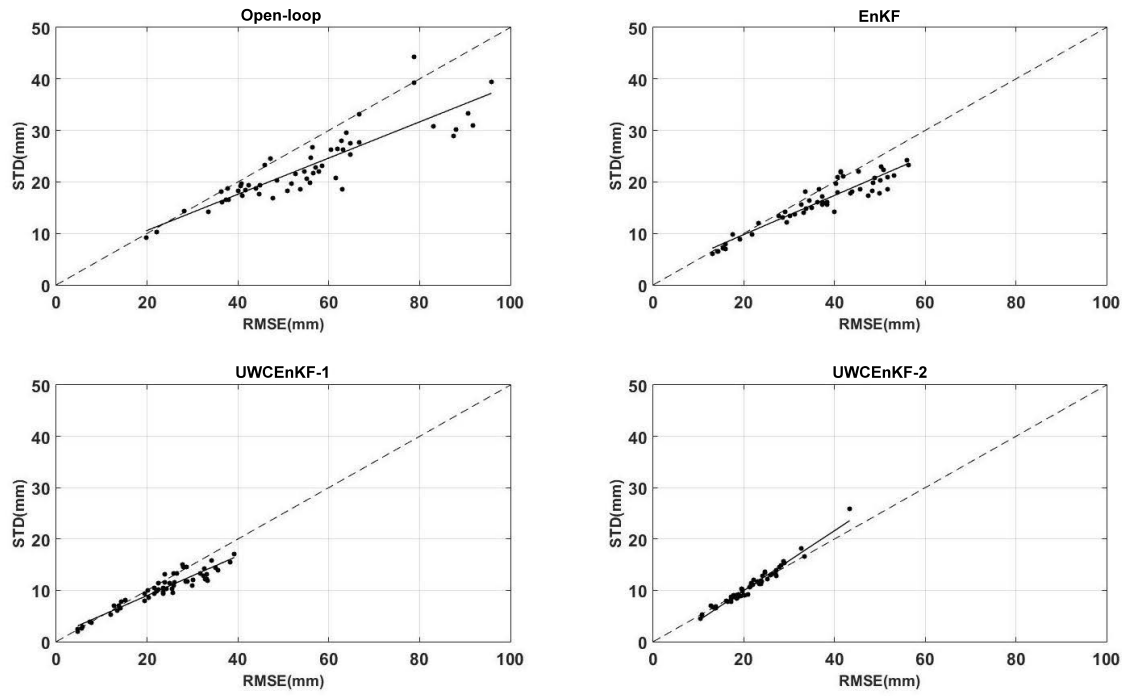


Figure 11: Average RMSE and STD of the groundwater results from the EnKF, UWCEnKF-1, and UWCEnKF-2 filters over the Murray-Darling basin regarding the in-situ groundwater measurements.

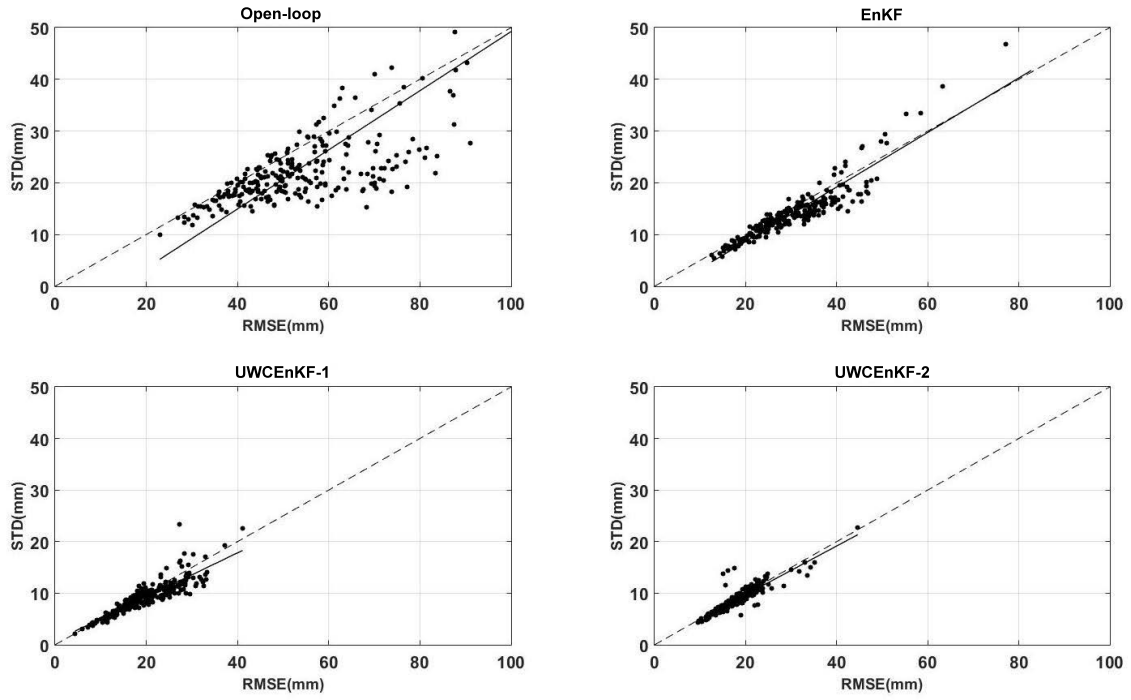


Figure 12: Average RMSE and STD of the groundwater results from the EnKF, UWCEnKF-1, and UWCEnKF-2 filters over the Mississippi basin regarding the in-situ groundwater measurements.

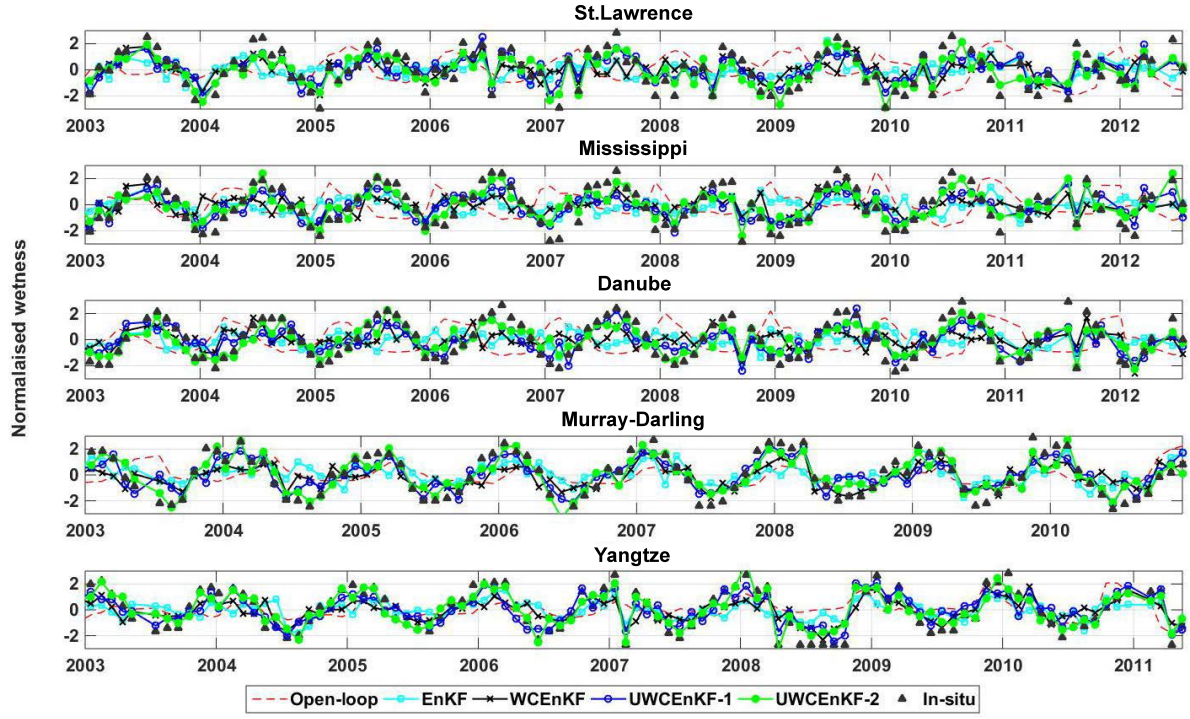


Figure 13: Average soil moisture variation time series by the open-loop run, EnKF, WCEnKF, UWCEnKF-1, and UWCEnKF-2 over St. Lawrence, Mississippi, Danube, Yangtze, and Murray-Darling basins.

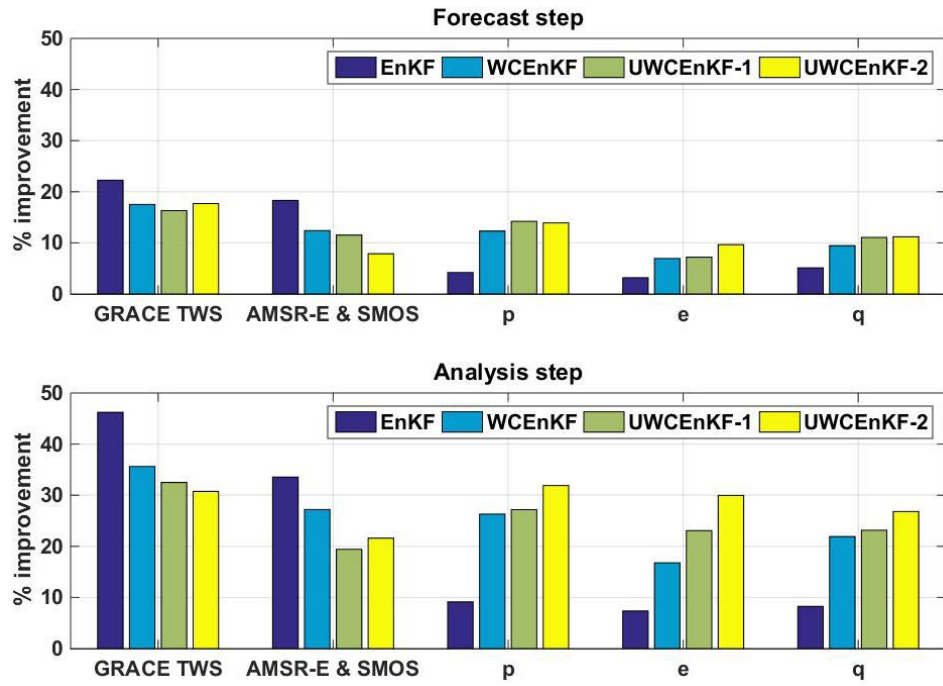


Figure 14: Average correlation improvements of filtered TWS time series to GRACE TWS,  $p$ ,  $e$ , and discharge  $q$  with respect to open-loop run in forecast and analysis steps. For AMSR-E+SMOS correlation, filtered top soil storage estimates are used.

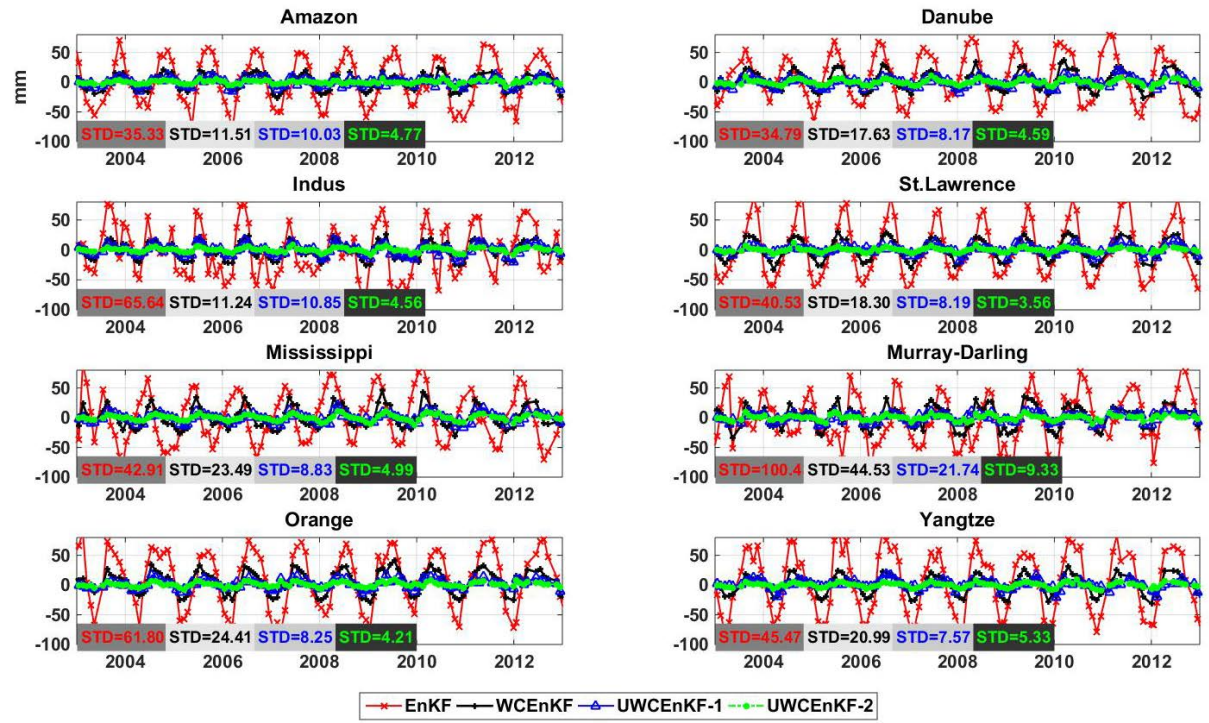


Figure 15: Average water budget imbalance time series calculated using EnKF, WCEnKF, and UWCEnKF variants for each basin (units are mm).



Table 1: A summary of the datasets used in this study.

Product	Platform	Reference
Terrestrial water storage (TWS)	GRACE	<a href="#">Mayer-Gürr et al. (2014)</a>
Soil moisture	AMSR-E	<a href="#">Njoku (2004)</a>
Soil moisture	SMOS	<a href="#">Draper et al. (2009)</a>
Precipitation ( <b>p</b> )	TRMM-3B42	<a href="#">Huffman et al. (2007)</a>
Precipitation ( <b>p</b> )	CMORPH	<a href="#">Joyce et al. (2004)</a>
Precipitation ( <b>p</b> )	GPCP	<a href="#">Adler et al. (2003)</a>
Precipitation ( <b>p</b> )	GPCC	<a href="#">Schneider et al. (2008)</a>
Precipitation ( <b>p</b> )	CPC	<a href="#">Chen et al. (2002)</a>
Evapotranspiration ( <b>e</b> )	MOD16	<a href="#">Mu et al. (2007)</a>
Evapotranspiration ( <b>e</b> )	GLEAM	<a href="#">Miralles et al. (2011)</a>
Evapotranspiration ( <b>e</b> )	ERA-interim	<a href="#">Simmons et al. (2007)</a>
Evapotranspiration ( <b>e</b> )	VIC	<a href="#">Liang et al. (1994)</a>
Water discharge ( <b>q</b> )	GRDC	<a href="http://www.bafg.de/GRDC/EN/Home/homepage_node.html">http://www.bafg.de/GRDC/EN/Home/homepage_node.html</a>
Water discharge ( <b>q</b> )		<a href="http://www.hydrosciences.fr/sierem/consultation/choixaccess.asp?lang=en">http://www.hydrosciences.fr/sierem/consultation/choixaccess.asp?lang=en</a>
Water discharge ( <b>q</b> )	USGS	<a href="https://waterdata.usgs.gov/nwis/sw">https://waterdata.usgs.gov/nwis/sw</a>
Water discharge ( <b>q</b> )		<a href="http://www.bom.gov.au/waterdata/">http://www.bom.gov.au/waterdata/</a>
Water discharge ( <b>q</b> )	NRFA	<a href="http://nrfa.ceh.ac.uk/data/">http://nrfa.ceh.ac.uk/data/</a>
Water discharge ( <b>q</b> )		<a href="http://www.ore-hybam.org/">http://www.ore-hybam.org/</a>
Water discharge ( <b>q</b> )		<a href="http://www.hydrology.gov.np/new/bull3/index.php/hydrology/home/main">http://www.hydrology.gov.np/new/bull3/index.php/hydrology/home/main</a>
Hydrological model	W3RA	<a href="http://www.wenfo.org/wald/data-software/">http://www.wenfo.org/wald/data-software/</a>
Groundwater in-situ measurements	NSW	<a href="http://waterinfo.nsw.gov.au/pinneena/gw.shtml">http://waterinfo.nsw.gov.au/pinneena/gw.shtml</a>
Groundwater in-situ measurements	USGS	<a href="https://water.usgs.gov/ogu/data.html">https://water.usgs.gov/ogu/data.html</a>
Soil moisture in-situ measurements	OzNet	<a href="#">Smith et al. (2012)</a>
Soil moisture in-situ measurements	ISMN	<a href="https://ismn.geo.tuwien.ac.at/">https://ismn.geo.tuwien.ac.at/</a>

Table 2: Average correlations between in-situ and soil moisture estimates from various methods. Improvements in the assimilation results are calculated as  $[(assimilation - open-loop\ run)/open-loop\ run] \times 100(\%)$ .

Basin	Open-loop	EnKF	WCEnKF	UWCEnKF-1	UWCEnKF-2
Danube	0.67	0.74	0.79	0.81	0.82
St. Lawrence	0.69	0.72	0.76	0.84	0.87
Mississippi	0.72	0.81	0.85	0.86	0.88
Murray-Darling	0.76	0.83	0.86	0.89	0.91
Yangtze	0.73	0.75	0.78	0.80	0.81
Improvements (%)	–	7.85	13.22	17.75	20.28

Table 3: Average correlations between the filtered water discharge and independent observations over different basins.

<b>Basin</b>	<b>Open-loop</b>	<b>EnKF</b>	<b>UWCEnKF-1</b>	<b>UWCEnKF-2</b>
Amazon	73.62	78.04	95.26	96.58
Danube	76.13	76.28	90.77	90.60
Indus	77.08	74.71	84.48	85.37
St. Lawrence	68.55	80.65	87.41	89.17
Mississippi	71.91	73.78	94.29	93.32
Murray-Darling	79.36	83.12	96.31	96.89
Orange	69.47	71.82	93.42	94.05
Yangtze	71.15	75.49	92.69	93.91